Bio-Design and Manufacturing (2026) 9:539–562
https://doi.org/10.1631/bdm.2500380

RESEARCH ARTICLE

A clinically guided photocurable hydrogel platform for antimicrobial peptide substitution in personalized wound infection therapy

Xiaolong Lin[1] · Tao Fu[2] · Yuqing Lei[3] · Jiajia Xu[1] · Haihua Zhu[1] · Fudong Zhu[1]

Received: 24 July 2025 / Accepted: 16 October 2025 / Published online: 10 April 2026

Abstract

The healing of infected skin wounds remains a major clinical challenge due to persistent bacterial contamination and prolonged inflammation. In this study, we report the development of a multifunctional, light-curable sodium alginate-based hydrogel by grafting antimicrobial peptides (AMPs) onto oxidized sodium alginate (OSA) via Schiff base reactions and incorporating silver nanoparticles (AgNPs). The dual-network hydrogel, formed by blending AMP@OSA with methacrylated alginate (AlgMA) and subsequent ultraviolet (UV) curing, exhibited a pH-responsive release behavior targeting the acidic microenvironment of infected wounds. In vitro studies demonstrated strong antibacterial activity against *Staphylococcus aureus* and *Escherichia coli*, significant inhibition of biofilm formation, and excellent biocompatibility, evidenced by minimal cytotoxicity and hemolysis. Treatment of a rat dorsal full-thickness infected wound model with the AMP-AgNPs@OSA hydrogel markedly accelerated wound closure, enhanced re-epithelialization, and promoted collagen deposition. Mechanistically, the hydrogel modulated the immune microenvironment by inducing macrophage polarization toward the anti-inflammatory M2 phenotype, thereby mitigating inflammatory responses and supporting tissue regeneration. These findings establish AMP-AgNPs@OSA hydrogel as a multifunctional dressing capable of simultaneously controlling infection and promoting wound repair, with strong potential for advanced clinical use in the management of infected skin defects. Moreover, the antimicrobial peptide component can be flexibly replaced with clinically appropriate antibiotics based on antimicrobial susceptibility testing, allowing personalized infection control and expanding the hydrogel's translational relevance across diverse pathogens.

Xiaolong Lin, Tao Fu, and Yuqing Lei have contributed equally to this work.

✉ Haihua Zhu
zhuhh403@zju.edu.cn

✉ Fudong Zhu
zfd@zju.edu.cn

[1] Stomatology Hospital, School of Stomatology, Zhejiang University School of Medicine, Zhejiang Provincial Clinical Research Center for Oral Diseases, Zhejiang Key Laboratory of Oral Biomedical, Engineering Research Center of Oral Biomaterials and Devices of Zhejiang Province, Hangzhou 310000, China

[2] Department of Oral and Maxillofacial Surgery, The Second Affiliated Hospital of Zhejiang University School of Medicine, School of Stomatology, and Key Laboratory of Oral Biomedical Research of Zhejiang Province, Hangzhou 310006, China

[3] Department of Minimally Invasive Interventional Radiology, The Second Affiliated Hospital, School of Biomedical Engineering, Guangzhou Medical University, Guangzhou 510260, China

Graphical abstract

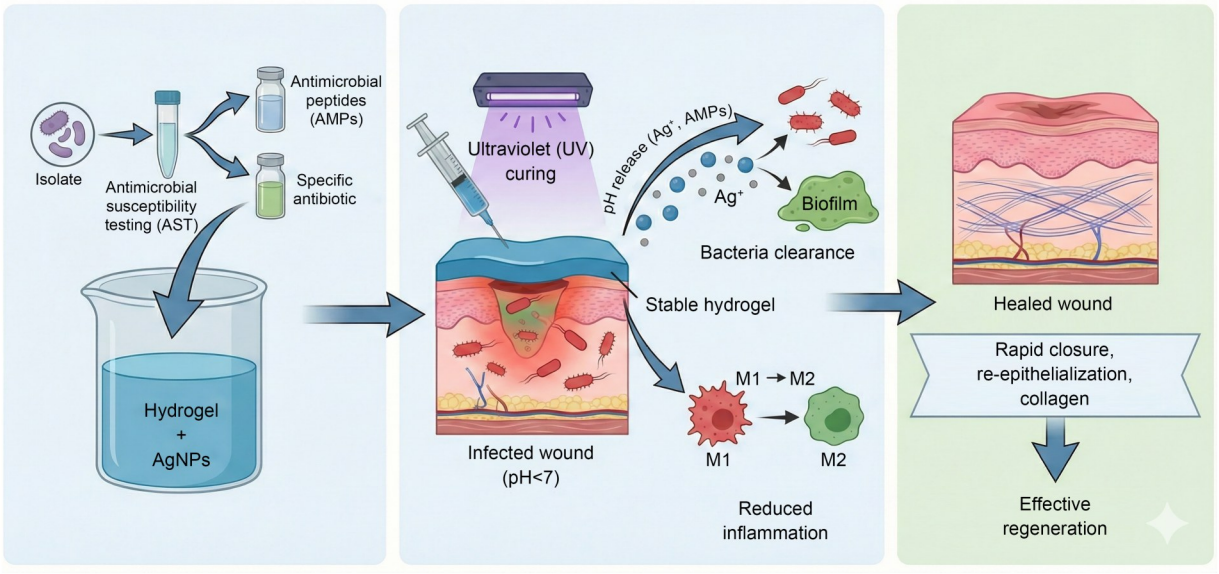

Keywords Antimicrobial peptide · Hydrogel · Wound healing · Anti-inflammatory

1 Introduction

The skin, the body's largest organ, serves as a physical barrier against external harm and participates in temperature regulation, sensory perception, and immune defense. Skin defects caused by trauma, surgery, burns, or chronic disease can severely compromise patients' quality of life. Timely and effective wound management is therefore essential to prevent infection, accelerate wound healing, reduce scarring, and restore skin function [1].

Infection is among the most common complications in complex wound healing [2], substantially delaying recovery and increasing treatment costs and patients' discomfort [3, 4]. Therefore, developing novel dressings that both control infection and promote wound healing is a key goal in biomaterials and skin repair research [5]. Among the various dressing materials, hydrogels are particularly promising due to their unique physicochemical properties and excellent biocompatibility [6]. Their high water content maintains a moist healing environment for wounds, supports drug loading and controlled release, reduces the number of dressing changes, and enhances comfort [7]. Numerous studies have demonstrated that nanocomposite hydrogels are valuable for skin defect repair [8, 9].

Sodium alginate (SA), a natural polysaccharide extracted from brown algae, is widely used in hydrogel preparation owing to its good biocompatibility, biodegradability, and gelation properties [10]. Alginate hydrogels can mimic the extracellular matrix and provide a favorable environment for cell growth and migration [11]. However, conventional alginate hydrogels have limited antimicrobial activity and modest effects on wound healing. Currently, hyaluronic acid (HA), SA, and gelatin methacrylate (GelMA) are commonly used as wound dressings in clinical practice. Recently, antimicrobial peptides (AMPs) have attracted increasing attention for their broad-spectrum antimicrobial activity, low resistance development, and immune-modulating properties. AMPs are small-molecule proteins found widely in nature and represent a key component of organisms' innate immune system. Incorporating AMPs into hydrogels can significantly enhance antimicrobial efficacy and reduce infection risk [12]. Silver nanoparticles (AgNPs) also exhibit potent antimicrobial properties [13]. Their high surface activity and nanoscale effects allow interaction with bacterial cell walls, disruption of bacterial metabolism, and induction of bacterial death. Additionally, AgNPs can promote wound healing and reduce inflammation [14, 15]. Although AMPs and metallic nanoparticles offer strong potential for infection control and wound healing [16], their effective integration and controlled release within hydrogels remain challenging [17]. Primarily, SA is selected as the base material due to its chemical tunability, biocompatibility, cost-effectiveness, and multifunctionality in treating infected skin defects [18]. SA dressings form gentle, moisture-retentive gels that are easily modified to incorporate bioactive molecules, thereby promoting cellular proliferation. Compared

with HA, which is costly and unstable, and GelMA, which requires complex processing and may contain solvent residue issues, SA demonstrates superior biocompatibility and controlled degradability—making it ideal for skin regeneration. Its easy oxidative modification, superior mechanical properties, and broad applicability further enhance its suitability for antibacterial, anti-inflammatory, and wound-healing hydrogel design [19]. Oxidized SA introduces aldehyde groups that readily bind AMPs via Schiff base reactions, forming a stable, chemically crosslinked network. Additionally, SA exhibits excellent pH responsiveness, enabling controlled AMP release under the acidic conditions typical of infected wounds, thereby improving antibacterial efficacy [20]. The natural abundance and low cost of SA, compared with HA and GelMA, make it particularly suitable for large-scale production and clinical application.

Wound healing is a complex biological process involving interactions among multiple cell types and signaling pathways [21]. Macrophages play a central role by clearing pathogens and necrotic tissue, regulating inflammation, and promoting tissue repair through cytokine secretion [22]. They can polarize into distinct phenotypes in response to microenvironment changes, with M1 (pro-inflammatory) and M2 (anti-inflammatory) being the two major polarization states [23]. Promoting macrophage polarization toward the M2 phenotype therefore reduces inflammation and accelerates wound healing [24].

This study developed a novel composite hydrogel system comprising two functional components: AMP-conjugated oxidized sodium alginate (AMP@OSA) and methacrylated alginate (AlgMA). These components form the hydrogel's structural basis, whereas AgNPs were incorporated to enhance antimicrobial and wound-healing performance, yielding a multifunctional dressing with robust therapeutic potential. This study investigated the hydrogel's preparation, physicochemical properties, antibacterial activity, wound healing efficacy, and influence on macrophage polarization. The findings provide a scientific basis for developing high-efficiency wound dressings and are expected to improve the clinical outcomes in infected skin defect treatment.

2 Materials and methods

2.1 Preparation of photocurable sodium alginate-based composite hydrogel

2.1.1 Preparation of oxidized sodium alginate

SA was dissolved in deionized water to prepare a 2% (20 g/L) solution. Sodium periodate ($NaIO_4$) was added at a molar ratio of 1:1 ($NaIO_4$ to sugar units in SA) and stirred under light-protected conditions at room temperature for 4 h. Ethylene glycol was then added to terminate the reaction, followed by dialysis against deionized water for 48 h using a 3500 Da molecular-weight-cutoff (MWCO) dialysis bag, with frequent water changes. The final product was freeze-dried to yield powdered oxidized SA (OSA).

2.1.2 Schiff base reaction between OSA and AMP

OSA was dissolved in deionized water to prepare a 2% (20 g/L) solution and mixed with human β-defensin-2 (hBD2, 100 μg/mL) solution at a 1:1 volume ratio. The mixture was stirred at pH 7.0 with 1 mol/L NaOH under light-protected conditions at room temperature for 4 h to form the AMP@OSA solution. This reaction involved condensation between aldehyde groups in OSA and amino groups in AMP, forming stable Schiff base bonds that ensure successful conjugation. The product was dialyzed against deionized water for 48 h using a 3500 Da MWCO dialysis bag with frequent water changes, and then freeze-dried to obtain powdered AMP@OSA.

2.1.3 AlgMA preparation

Unsaturated double bonds were introduced into SA AlgMA via an esterification reaction between methacrylic anhydride (MA) and hydroxyl groups on the SA side chain (Scheme 1a). Sodium alginate (500 mg) was completely dissolved in ultra-pure water to prepare a 2% (mass fraction) solution by stirring for 4 h at room temperature. N,N-dimethylformamide (DMF) was added dropwise (water: DMF=3: 2, volume ratio) and stirred well, and the mixture was cooled to 4 °C. MA was then added at a molar ratio of MA: SA=3: 1, and the reaction proceeded for 24 h at pH 8–9, maintained with 0.5 mol/L NaOH. The polymer was precipitated with ethanol, dissolved in ultra-pure water, and dialyzed for 3 d (MWCO= 14 kDa). The purified sodium alginate derivative was recovered by freeze-drying for later use.

2.1.4 Incorporation of AgNPs

A 0.02% (0.2 g/L) AgNPs solution was prepared and ultrasonicated for 10 min to achieve uniform dispersion. The AgNPs solution was added to the AMP@OSA and AlgMA mixture and thoroughly stirred to ensure homogeneous distribution of nanoparticles.

2.1.5 Preparation of two-component hydrogel

The concentration of the AMP@OSA solution was adjusted to 3% (30 g/L) and AlgMA to 5% (50 g/L). The two solutions were mixed at a 3:7 (mass ratio) AMP@OSA:AlgMA ratio. Irgacure 2959 (I2959) was added as a photoinitiator at a final concentration of 0.1% (1 g/L). The mixture was stirred until homogeneous to prevent phase separation.

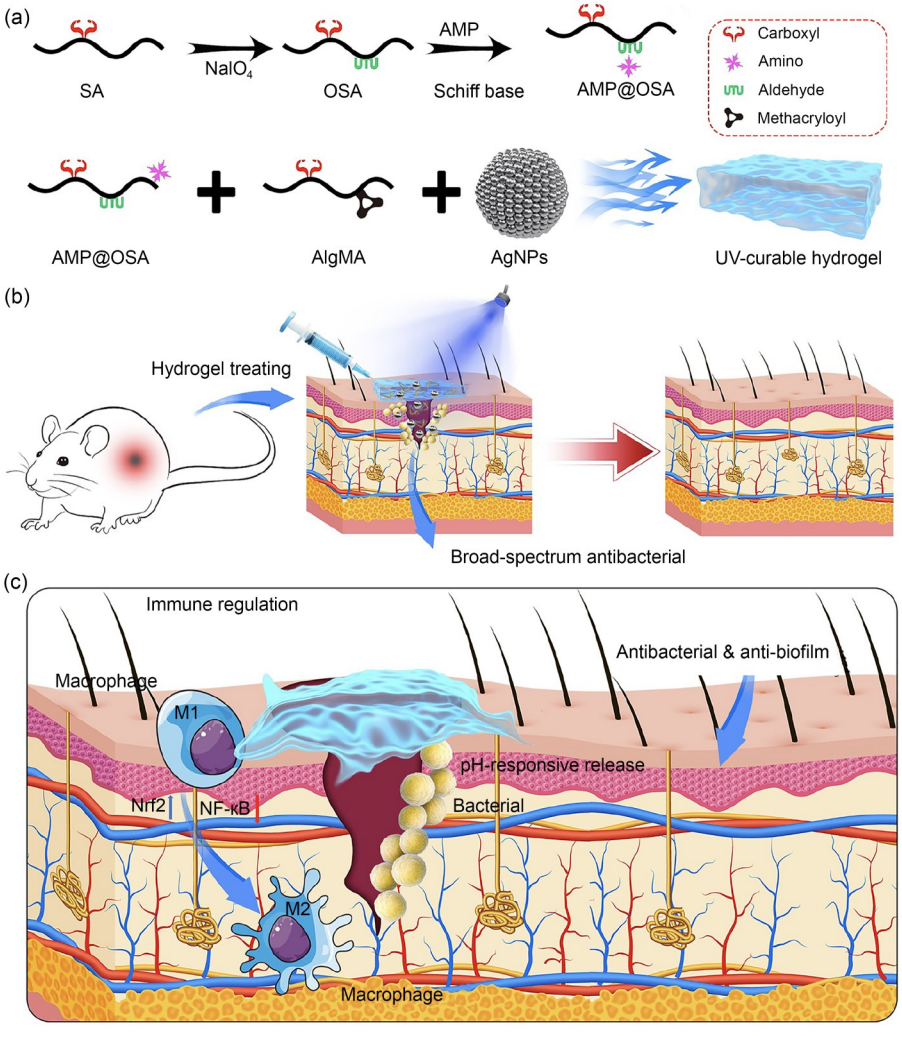

Scheme 1 Schematic illustration of the design, synthesis, and mechanism of the UV-curable pH-responsive sodium alginate hydrogel for infected wound healing. (a) AMP@OSA was first prepared via a Schiff base reaction, and the composite hydrogel was then formed by crosslinking with AlgMA and AgNPs under UV irradiation. (b) Application of the hydrogel on infected wounds, enabling pH-responsive AMP release and broad-spectrum antibacterial activity. (c) Biological effects of the hydrogel, including immunomodulation, antibacterial action, and biofilm inhibition, in facilitating wound healing

2.1.6 Photo-crosslinking and hydrogel formation

The final mixture was cast into molds or applied to the desired surface and photo-crosslinked under ultraviolet (UV) light (365 nm, 5–10 mW/cm^2). Curing lasted 5–15 min, depending on the hydrogel thickness. The dual-network hydrogel exhibited the desired mechanical and functional properties.

2.2 Quality control and manufacturability evaluation of the hydrogel system

2.2.1 Aldehyde content determination

The oxidation degree of SA was determined by quantifying aldehyde groups using the hydroxylamine hydrochloride titration method. Briefly, OSA samples were incubated with hydroxylamine hydrochloride in an acidic medium, and the released HCl was titrated with standardized NaOH. The aldehyde content was calculated from the titration volume and expressed as mmol/g. Three independent batches were measured to assess batch-to-batch consistency.

2.2.2 Grafting efficiency of antimicrobial peptides

The grafting efficiency of the AMPs onto OSA was assessed by measuring the residual unbound peptides in the supernatant after the Schiff base reaction. The initial peptide concentration in the reaction system was defined as C_{total}, whereas the concentration of free, unreacted peptides remaining in the supernatant was determined as C_{free} using a bicinchoninic acid protein assay. Grafting efficiency (η_g) was calculated as follows:

$$\eta_g=(1-C_{free}/C_{total})\times 100\%.$$

A higher grafting efficiency indicated a greater proportion of peptides immobilized within the hydrogel network.

2.2.3 AgNPs characterization

The average size and polydispersity index (PDI) of in situ synthesized AgNPs within the hydrogel matrix were analyzed via dynamic light scattering (DLS, Zetasizer Nano-ZS, Malvern Panalytical, UK). Hydrogels were diluted in deionized water before measurement, and data from three independent batches were analyzed.

2.2.4 Microstructure and pore size distribution

Freeze-dried hydrogel scaffolds were sectioned and sputter-coated with gold. Scanning electron microscopy (SEM) images were obtained under low vacuum at 5 kV. Porosity was calculated using image threshold analysis via ImageJ, and pore size distribution was measured from over 100 randomly selected pores per sample.

2.2.5 Injectability testing

The hydrogel precursor solution was loaded into syringes fitted with 18G, 21G, or 23G needles. A TA-XTplus texture analyzer (Stable Micro Systems, Godalming, UK) applied compression at 1 mm/s, and the peak extrusion force was recorded for each needle type. Each configuration was tested in triplicate.

2.2.6 Rehydration efficiency after lyophilization

Hydrogels were lyophilized and stored for 1 month at − 40, − 20, 4, 15, or 25 °C. Rehydration was initiated by adding 1 mL phosphate-buffered saline (PBS) to each sample and vortexing until uniform dispersion was achieved. The rehydration rate was calculated as the percentage of recovered mass compared with the pre-lyophilization weight.

2.3 Hydrogel characterization

The chemical composition of the hydrogel membranes was characterized using Fourier transform infrared spectrophotometry (FTIR, Bruker Vector 22, Germany), with samples blended in a potassium bromide pellet and spectra acquired over 64 scans at a resolution of 4.0 cm^{-1}, and by proton nuclear magnetic resonance (^1H NMR) spectroscopy (Bruker AVANCE III 500, Germany; 40 °C in deuterated H_2O). Hydrogel surface morphology was examined using field-emission SEM (Nova Nano 450, Thermo FEI, Czech Republic) at an accelerating voltage of 5 kV after platinum sputtering, and elemental composition was assessed using energy-dispersive X-ray spectroscopy (EDX). Crystallinity was analyzed using X-ray diffraction (XRD) with Cu Kα radiation (λ =1.5406 Å; 1 Å = 1×10^{-10} m) at 40 kV and 30 mA, a scanning range of 5°–80° (2θ) at 2 (°)/min. Hydrogel surface chemical bond changes were further characterized using X-ray photoelectron spectroscopy (AXIS Supra, Kratos, UK). Spectral data were processed using ESCApe software (Kratos Analytical, Manchester, UK), with the C 1s photoelectron peak at 284.8 eV as the binding-energy reference.

2.3.1 Differential scanning calorimetry

The thermal properties of lyophilized hydrogels were analyzed using differential scanning calorimetry (DSC) under a nitrogen atmosphere (flow rate: 50 mg/min). Approximately 10 mg of each sample was heated at 10 °C/min, and the corresponding thermal transitions were recorded.

2.3.2 Adhesion performance

Surface hydrophilicity and wet adhesion properties of the SA hydrogel were evaluated using a contact angle goniometer. The hydrogel was freeze-dried into a uniform flat film, and measurements were performed with either deionized water or simulated body fluid as the testing liquid. The film was mounted on the measurement stage, and a droplet was placed on its surface. The droplet's contact angle was captured and analyzed using software, whereby an angle <90° indicated hydrophilicity. Dynamic contact angle changes, including droplet spreading or absorption, were also recorded to assess wet adhesion performance. Each sample was tested in triplicate, and contact angle trends were analyzed to determine hydrophilic and adhesive performance.

2.3.3 Swelling performance test

The swelling properties of freeze-dried hydrogel scaffolds were evaluated gravimetrically. Each hydrogel was weighed on an analytical balance to obtain its initial dry weight (W_a), and then immersed in PBS at 37 °C to monitor swelling over time. Samples were collected at 2, 4, 10, 12, 24, 48, and 72 h, and excess surface water was gently removed with filter paper before reweighing (W_b). Each group included three replicate samples. The hydrogel swelling degree (W) was calculated as follows:

$$W=\frac{W_b-W_a}{W_a}\times100\%.$$

The swelling ratio reflects the hydrogel's water absorption capacity and structural stability.

2.3.4 AMP and AgNP release tests

AMP release behavior was evaluated by immersing the hydrogel samples in 2 mL PBS at 37 °C with continuous shaking. At predetermined time points (1, 3, 5, 7, 9, and 14 d), 1 mL of release medium was withdrawn for analysis and

replaced with an equal volume of fresh PBS. AMP concentration in the release medium was determined using a microplate reader at 270 nm, and the cumulative release rate (r_{cr}) was calculated with the following formula:

$$r_{cr}=\frac{C_t}{C_\infty}\times 100\%,$$

where C_t represents the AMP concentration released at time t and C_∞ is the total AMP amount encapsulated in the AMP-AgNPs@OSA hydrogel.

For AgNPs release tests, hydrogel samples were immersed in 10 mL PBS at 37 °C and shaken at 50 r/min. Supernatant aliquot (100 μL) was collected at 0, 1, 3, 5, 7, 9, and 14 d, filtered, and stored for analysis; equal volumes of fresh PBS were replenished after sampling. Atomic absorption spectroscopy was used to determine the concentration of silver ions in the supernatant. The results were plotted as a release curve; the release rate per unit time and the cumulative release were calculated, and the release kinetics of silver nanoparticles over time were analyzed.

2.3.5 Thermogravimetric analysis

Samples (5–10 mg) were evenly distributed in crucibles for analysis under an air atmosphere (flow rate: 20–50 mL/min) using a heating rate of 10 °C/min from room temperature to 800 °C. The thermogravimetric analysis (TGA) instrument recorded the mass–temperature curve to assess water loss, decomposition temperature, and residual mass. Uniform sample preparation, moderate heating rates, and regular instrument calibration ensured data accuracy.

2.3.6 Injectable capacity

Freshly prepared hydrogel samples were loaded into 1 mL syringes and injected into glass culture dishes imprinted with the text "ZJU" and a spiral pattern to visually evaluate injectability. Following UV curing, the hydrogel was examined to confirm its photocuring ability and shape fidelity.

2.4 In vitro biodegradation tests

The biodegradation of the dual-network hydrogel was assessed by incubating samples in degradation media at 37 °C. Uniform-sized hydrogel discs were prepared, dried, and weighed (W_0). Samples were immersed in 10 mL PBS (pH 7.4) with or without lysozyme (1 mg/mL, 10 000 U/mL) to simulate physiological and enzymatic conditions. The hydrogels were incubated at 50 r/min and retrieved at 1, 3, 7, 14, and 21 d. After gentle rinsing and blotting, the wet weights (W_t) were recorded. Weight loss was calculated as $(W_0-W_t)/W_0\times 100\%$. Degradation behavior was assessed by monitoring structural and morphological changes, including optional surface examination using SEM. This analysis elucidated the degradation profiles under enzymatic and non-enzymatic conditions, confirming the hydrogel's biomedical applicability.

2.4.1 Cell viability evaluation

NIH/3T3 fibroblasts were selected as test cells, seeded in 96-well plates at 5×10^3 cells/well, and cultured with leachates from OSA and AMP-AgNPs@OSA hydrogels (100 μg/mL). The control group received no leachate, and PBS served as the blank. Cell cytotoxicity and proliferation were measured using the Cell Counting Kit-8 (CCK-8, Dojindo Laboratories, Kumamoto, Japan) at 48 and 96 h. After 2 h of incubation with CCK-8 reagent at 37 °C, absorbance was measured at 450 nm using a microplate reader (Multiskan MK3, Thermo Fisher Scientific, Waltham, MA, USA).

Cell compatibility was further assessed using a Live/Dead Cell Staining Kit (Solarbio, Beijing, China). NIH/3T3 cells (2×10^4 cells/well) were cultured in 24-well plates under identical conditions. Calcein acetoxymethyl ester (Calcein-AM) and propidium iodide (PI) were used to stain live (green) and dead (red) cells, respectively, at 48 and 96 h following the manufacturer's instructions. Samples were visualized using fluorescence microscopy (Zeiss LSM 710, Carl Zeiss, Germany).

2.4.2 Hemolysis test

A hemolysis assay was performed to evaluate the hydrogel's blood compatibility. Fresh anticoagulated rabbit blood was centrifuged to isolate red blood cells (RBCs), which were washed and resuspended in saline to obtain a 2% suspension. Hydrogel extract solutions were incubated with RBCs at 37 °C for 1 h. Saline and 0.1% Triton X-100 served as negative and positive controls, respectively. After centrifugation, the absorbance of the supernatant was measured at 540 nm to quantify hemolysis. The hemolysis rate (r_h) was calculated as follows:

$$r_h=\frac{OD_{test}-OD_{neg}}{OD_{pos}-OD_{neg}}\times 100\%,$$

where OD_{test}, OD_{neg}, and OD_{pos} denote the absorbance values of the test sample, negative control, and positive control, respectively. A hemolysis rate below 5% was considered indicative of good hemocompatibility.

All data were statistically analyzed using one-way analysis of variance (ANOVA) and visualized with GraphPad Prism, ensuring reproducibility and robust assessment of hydrogel blood safety.

2.4.3 Antibacterial activity test

Plate colony count: *Staphylococcus aureus* ATCC 25923 (*S. aureus*) and *Escherichia coli* ATCC 25922 (*E. coli*)

were cultured overnight in nutrient agar. For each group (control, OSA, AMP-AgNPs@OSA), bacterial suspensions (100 μL, 1×10^6 CFU/mL; CFU: colony-forming unit) were spread evenly on agar plates. After 24 h of incubation at 37 °C, colonies were counted using an automatic colony counter, and antibacterial activity was determined by comparing colony counts among groups.

Crystal violet biofilm formation assay: Biofilm formation was quantified using crystal violet staining. Bacterial suspensions (100 μL, 1×10^6 CFU/mL) of *S. aureus* and *E. coli* were added to 96-well plates containing control, OSA, or AMP-AgNPs@OSA hydrogels. Following 24 h of incubation at 37 °C, non-adherent bacteria were removed via PBS washing, and biofilms were stained with 0.1% crystal violet solution for 20 min. Excess stain was rinsed off, and biofilms were solubilized in 95% ethanol. Absorbance was read at 570 nm using a microplate reader to quantify biofilm biomass.

Confocal laser scanning microscopy for biofilm live/dead staining: Live/Dead staining of biofilms formed by *S. aureus* and *E. coli* on control, OSA, and AMP-AgNPs@OSA hydrogels was performed using the LIVE/DEAD BacLight Bacterial Viability Kit (Invitrogen, Thermo Fisher Scientific) according to the manufacturer's instructions. Biofilms were stained with SYTO 9 (green, live cells) and PI (red, dead cells) and incubated in the dark for 15 min. Biofilm images were captured using a confocal laser scanning microscope (Zeiss LSM 710, Carl Zeiss) at excitation wavelengths of 488 nm (SYTO 9) and 633 nm (PI).

2.5 Transcriptomic analysis of NIH/3T3 cells

NIH/3T3 fibroblasts were cultured in Dulbecco's modified Eagle medium (DMEM) containing 10% fetal bovine serum (FBS) and 1% penicillin-streptomycin at 37 °C under 5% CO_2. Cells were seeded in six-well plates (1×10^6 cells/well) and treated with AMP-AgNPs@OSA hydrogel extract for 24 h; untreated cells served as controls. Total RNA was extracted using TRIzol, and RNA integrity was assessed using a Nanodrop spectrophotometer (Thermo Fisher Scientific) and an Agilent 2100 Bioanalyzer (Agilent Technologies, Santa Clara, CA, USA). Libraries were constructed and sequenced using an Illumina NovaSeq 6000 platform. Clean reads were aligned to the mouse genome, and differentially expressed genes (DEGs) were identified using DESeq2 ($|\log_2FC|>1$, $p<0.05$). Functional enrichment was conducted via Gene Ontology and Kyoto Encyclopedia of Genes and Genomes (KEGG) analyses to elucidate anti-inflammatory mechanisms. Principal component analysis and heatmaps were generated for visualization, with multiple-testing corrections applied using the Benjamini–Hochberg method.

2.6 Macrophage polarization assay

RAW 264.7 macrophages were cultured in DMEM with 10% FBS and 1% penicillin-streptomycin at 37 °C under 5% CO_2. Cells were seeded in six-well plates (1×10^6 cells/well) and treated for 24 h with lipopolysaccharide (LPS, 100 ng/mL) for M1 polarization, interleukin (IL)-4 (20 ng/mL) for M2 polarization, OSA hydrogel extract, or AMP-AgNPs@OSA hydrogel extract. For immunofluorescence staining, cells were fixed, permeabilized, and incubated with primary antibodies against cluster of differentiation 206 (CD206, M2 marker) and inducible nitric oxide synthase (iNOS, M1 marker), followed by fluorescent secondary antibodies. Nuclei were counterstained with 4',6-diamidino-2-phenylindole (DAPI), and images were obtained using confocal microscopy. For flow cytometry, cells were harvested, stained with fluorescently labeled anti-CD86 (M1) and anti-CD206 (M2) antibodies, and analyzed using a FACS instrument to quantify macrophage subpopulations. For Western blotting, total protein was extracted, separated using sodium dodecyl sulfate-polyacrylamide gel electrophoresis, and transferred to polyvinylidene membranes. Primary antibodies were used to target CD86, iNOS (M1 markers), arginase-1 (Arg-1), and CD206 (M2 markers); β-actin served as the loading control. Protein bands were visualized via chemiluminescence and quantified using ImageJ. Reverse transcription-quantitative polymerase chain reaction (RT-qPCR) was performed to measure the expression of CD86, iNOS (M1 markers), Arg-1, and CD206 (M2 markers). Glyceraldehyde-3-phosphate dehydrogenase (GAPDH) served as the internal control. Gene expression was quantified using the $\Delta\Delta C_t$ method. Primer sequences are listed in Table 1.

2.7 In vivo models

To evaluate the in vivo therapeutic efficacy of the AMP-AgNPs@OSA hydrogels, a standardized full-thickness skin defect model was established.

The wound-healing efficacy of the AMP-AgNPs@OSA hydrogel was assessed using an infected full-thickness skin defect model in Sprague–Dawley (SD) rats. Thirty-six female SD rats (200–250 g) were obtained from Shanghai Slack Experimental Animal Company (Shanghai, China) and maintained under standard laboratory conditions (12-h light/dark cycle) with free access to water and food. Animals were randomly divided into Control, OSA, and AMP-AgNPs@OSA hydrogel treatment groups. The Institutional Animal Care and Use Committee approved all procedure protocols. Full-thickness skin defects (approximately 1.5 cm in diameter) were created on the dorsal side of each rat using a sterile 15-mm biopsy punch. Each wound was inoculated with *S. aureus* suspension (10^6 CFU/mL) to induce infection, followed by treatment initiation on Day 0. Approximately 100 μL of AMP-AgNPs@OSA hydrogel was applied to the wound,

Table 1 Primers used for RT-PCR analysis

Gene	Primer direction	Primer sequence
iNOS	Forward	5'-CAACAGGGAGAAAGCGCAAA-3'
	Reverse	5'-ATTCTGTGCTGTCCCAGTGAG-3'
CD86	Forward	5'-CCACGATGGACCCCAGATG-3'
	Reverse	5'-CCTTTGTAAATGGGCACGGC-3'
CD206	Forward	5'-ACGAGCAGGTGCAGTTTACA-3'
	Reverse	5'-ACATCCCATAAGCCACCTGC-3'
Arg-1	Forward	5'-GTGAAGAACCCACGGTCTGT-3'
	Reverse	5'-AGAAAGGACACAGGTTGCCC-3'
β-actin	Forward	5'-GACTGTTACTGAGCTGCGTTT-3'
	Reverse	5'-ACTTTGGGGGATGTTTGCTC-3'

whereas OSA hydrogel or saline solution was applied in the corresponding control groups. Treatments were renewed every 2 d until Day 12, and wound healing progression was documented on Days 0, 2, 5, 7, 10, and 12.

Body weights were recorded on Days 0, 2, 5, 7, 10, and 12 using a digital balance to monitor animal health. On Days 2 and 7, bacterial samples were collected from each rat for quantification using quantitative PCR (qPCR). Photographs were taken at each time point to assess wound contraction and healing progression. The wound area was measured using digital imaging software, and wound contraction was quantified relative to the initial wound size (Day 0). Wound healing was monitored by evaluating time-dependent changes in wound size, which were then statistically analyzed. Rats were euthanized on Day 12, and their skin tissues were harvested for histological analysis. Hematoxylin and eosin (H&E) staining was used for morphological assessment, Masson's trichrome for collagen deposition, and immunohistochemistry for IL-10 and IL-6 to evaluate the inflammatory response at the wound site.

2.8 Statistical analysis

All quantitative data are expressed as mean±standard deviation from at least three independent replicates. Statistical analyses were performed using GraphPad Prism 9.0. Two groups were compared using an unpaired two-tailed Student's *t*-test, while multiple comparisons were analyzed using one-way ANOVA followed by Tukey's post hoc test. Non-normally distributed data were analyzed using the Kruskal-Wallis test with Dunn's multiple comparisons. Statistical thresholds were set at $^{*}p<0.05$, $^{**}p<0.01$, and $^{***}p<0.001$.

3 Results and discussion

3.1 Manufacturing consistency and functional performance of the hydrogel system

The synthesis of the hydrogel material and its biological performance are presented in Scheme 1. The chemical synthesis of the hydrogels is illustrated in Fig. S1 (supplementary information). As illustrated in Fig. 1a, the hydrogel system exhibits a modular, clinically adaptable design. OSA provides reactive aldehyde groups that form Schiff base linkages, enabling efficient and stable immobilization of AMPs. AlgMA, synthesized through carbodiimide-mediated chemistry, introduces photoreactive double bonds for rapid UV-induced gelation, allowing in situ application. To ensure reproducibility, quantitative quality-control parameters were established across three independent fabrication batches. The oxidation degree of SA remained consistent, with aldehyde contents of (3.5±0.04) mmol/g (Fig. 1b), demonstrating excellent process consistency. The Schiff base conjugation efficiency for AMP immobilization reached (82.5±0.5)% (Fig. 1c).

AgNPs incorporation exhibited uniform distribution with a mean diameter of 100 nm and a low PDI (0.16±0.01), confirmed using DLS (Fig. 1d). The lyophilized hydrogel displayed a porous microarchitecture (average porosity: (72.3±2.1)%; pore size: 20–60 μm; Figs. 1e and 1f), which supports nutrient diffusion and cellular infiltration—key factors in wound healing.

From a translational perspective, the hydrogel demonstrated excellent injectability, requiring a manual injection force of 4.6 N through a 21G needle (Fig. 1g), suitable for clinical application. Lyophilized hydrogel powders retained >91% rehydration capacity after a 1-month storage, with optimal recovery at −20–4 °C (Fig. 1h), indicating strong storage stability and convenience for point-of-care deployment.

Overall, the hydrogel system showed robust and controllable synthesis, as evidenced by the consistent aldehyde content, stable peptide grafting efficiency, and uniform AgNPs dispersion across multiple batches. Its well-defined pore structure facilitates cellular infiltration and nutrient exchange, while its injectability through standard clinical needle gauges and excellent rehydration performance after lyophilization favor practical, on-demand application and long-term storage. Moreover, the dynamic Schiff base chemistry for antimicrobial peptide conjugation allows facile substitution of AMP

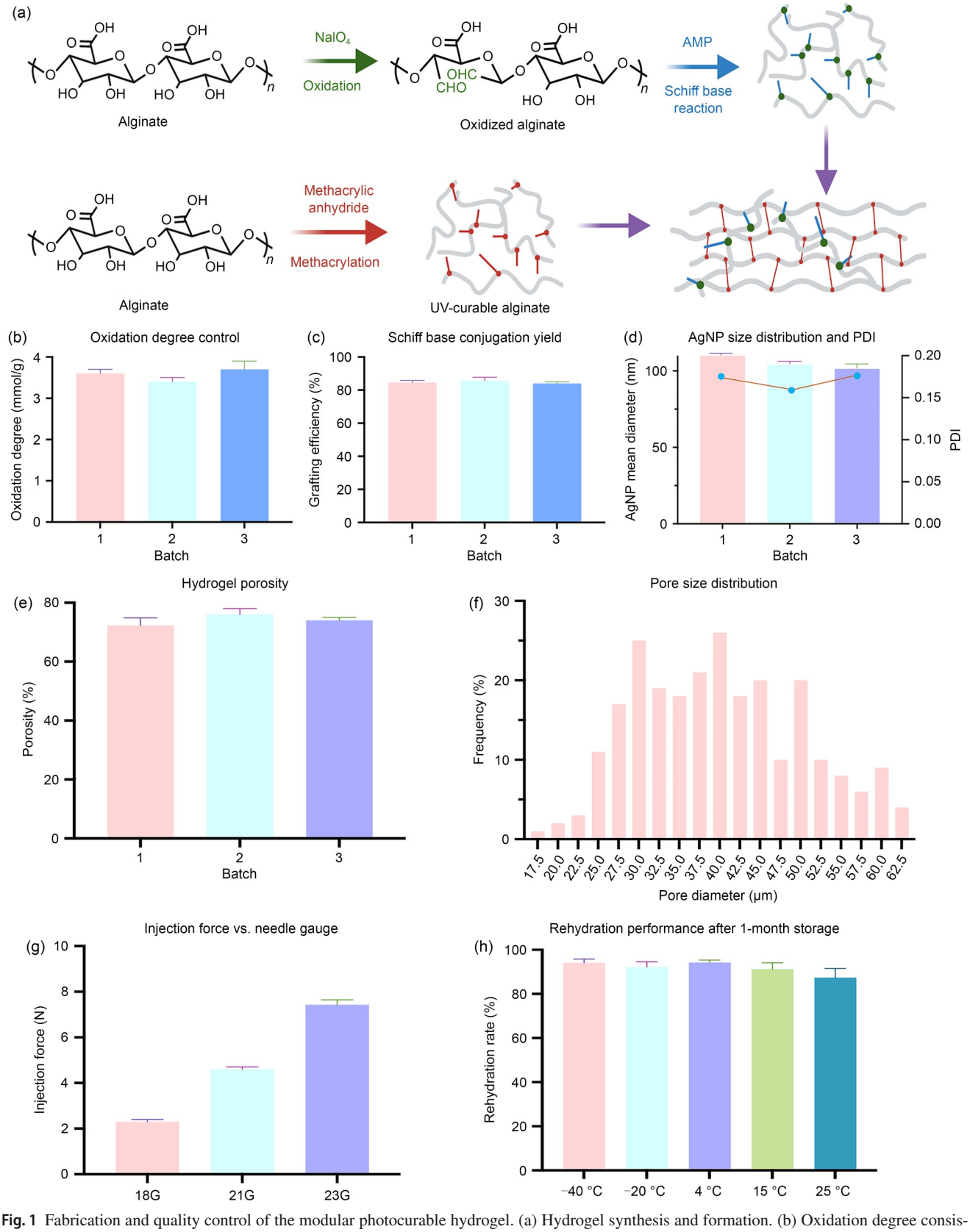

Fig. 1 Fabrication and quality control of the modular photocurable hydrogel. (a) Hydrogel synthesis and formation. (b) Oxidation degree consistency across batches. (c) AMP conjugation efficiency via Schiff base linkage. (d) Size and uniformity analysis of AgNPs. (e, f) Porosity and pore size distribution of the hydrogel. (g) Injection force evaluation for clinical handling. (h) Rehydration performance after storage under various temperatures. Data are presented as mean±standard deviation (n=3). PDI: polydispersity index

components according to patient-specific microbial profiles, supporting personalized antimicrobial therapy. These features highlight the hydrogel's scalability, precision, and potential for clinical wound management.

3.2 Enhanced structural characteristics and controlled release properties of AMP-AgNPs@OSA hydrogel

The FTIR spectra (Fig. 2a) revealed that SA exhibited a strong stretching vibration peak around 3400 cm^{-1}, corresponding to the O–H absorption band of hydroxyl groups in its side chains. Peaks near 1600 and 1410 cm^{-1} were attributed to the stretching vibrations of the carboxylate ($–COO^-$) groups, while the absorption band near 1030 cm^{-1} indicated the vibrational absorption of ether bonds within the sugar ring. The peak near 820 cm^{-1} represented the vibrational absorption of hydroxyl groups. The modified AlgMA retained these characteristic SA stretching vibration peaks, confirming that the primary SA structure remained unchanged after modification. A new vibrational absorption peak at 1720 cm^{-1} in AlgMA, corresponding to the C=O stretching vibration of ester bonds, confirmed the successful introduction of ester groups. Additionally, a peak at 1630 cm^{-1} was assigned to C=C stretching vibration, confirming the successful conjugation of MA to SA and the presence of polymerizable carbon-carbon double bonds, enabling photopolymerization. Modified OSA and AMP@OSA retained the key SA absorption peaks, suggesting structural preservation after modification. In OSA, a new peak at 1726 cm^{-1}, attributed to –CHO stretching vibration, confirmed successful oxidation of SA and the introduction of reactive aldehyde (–CHO) groups. In AMP@OSA, the peak at 3400 cm^{-1} shifted to a lower frequency, corresponding to aliphatic $–NH_2$ stretching, while a new band appeared at 890 cm^{-1} due to $–NH_2$ bending vibration, indicating the successful conjugation of AMPs to OSA.

The structures of SA, AlgMA, OSA, and AMP@OSA were characterized using ^1H NMR with D_2O as the solvent. Figure 2b shows that the peak at δ 4.79 ppm corresponded to the solvent signal, where δ denotes the chemical shift in parts per million (ppm, equivalent to 10^{-6}), whereas the resonances at δ 3.5–4.5 ppm were attributed to the characteristic sugar ring protons of SA. Compared with SA, AlgMA displayed new peaks at δ 5.73 ppm and δ 6.16 ppm (olefinic protons of MA) and at δ 1.93 ppm (methyl hydrogen adjacent to the amide group), confirming successful grafting of MA anhydride onto SA. OSA exhibited a new hemiacetal proton peak at δ 5.5 ppm, validating the successful introduction of aldehyde groups into SA through oxidation of the C2 and C3 hydroxyls. The chemical environment of the protons was altered, resulting in a new peak approximately δ 3.5 ppm, which persisted in OSA. In AMP@OSA, a distinct amide proton signal near δ 8.0 ppm confirmed successful AMP conjugation.

SEM images (Fig. 2c) revealed that OSA and AMP-AgNPs@OSA had significant microstructural differences. OSA displayed a relatively uniform, small-pore structure with a dense surface, suitable as a structural scaffold material for non-infected skin defects. In contrast, AMP-AgNPs@OSA showed an interconnected porous architecture with larger, irregularly distributed pores, a rougher surface, and more prominent crosslinks between pores conducive to cell migration and proliferation. Energy-dispersive spectroscopy (EDS) mapping confirmed the presence and uniform distribution of C, O, Na, Ag, and N elements in AMP-AgNPs@OSA, verifying the successful incorporation of AgNPs and AMPs within the OSA matrix. The detected Ag and N signals further validated AgNP and AMP loading, respectively. This well-organized porous structure supports antibacterial activity and wound healing, while AMP incorporation enhanced both pore structure diversity and functional drug-release capacity—crucial for inhibiting microbial growth, reducing inflammation, and promoting wound healing in infected skin defects.

The comparison of the SA structure and performance before and after modification indicated that the modification significantly altered the material's microstructure. Before modification, the XRD spectrum (Fig. 2d) of SA exhibited typical amorphous characteristics, with a broad peak between 20° and 30°, indicating that its internal structure was primarily amorphous. After modification, AgNP introduction generated new diffraction peaks in the 2θ range of 40°–45°, confirming the successful incorporation of AgNPs with crystalline structures. These structural modifications also altered SA chain spacing and reduced peak intensity, indicating molecular reorganization. XPS (Fig. 2e) further verified successful functionalization, revealing prominent N 1s (approximately 400 eV) and Ag 3d (approximately 368–374 eV) signals corresponding to AMP grafting and AgNP incorporation, respectively. The N 1s signal confirmed nitrogen introduction from the AMPs, whereas the Ag 3d signal indicated Ag presence. Shifts in the C 1s and O 1s peaks suggested possible Ag–O bond formation or coordination between AgNPs and peptide amino/carboxyl groups. Collectively, these results confirm that AMP and AgNP modification synergistically enhanced the hydrogel's structural integrity, antibacterial functionality, and long-term stability.

Figures 2f and 2g present the cumulative release profiles of AgNPs and AMPs from the hydrogel. Approximately 80% of Ag was released within 10 d, providing rapid initial antimicrobial action crucial for early-stage infection control. In contrast, AMP release exhibited pH-sensitivity—occurring significantly faster at pH 5.5 than at pH 7.4—allowing targeted release in acidic, infected wound environments. This

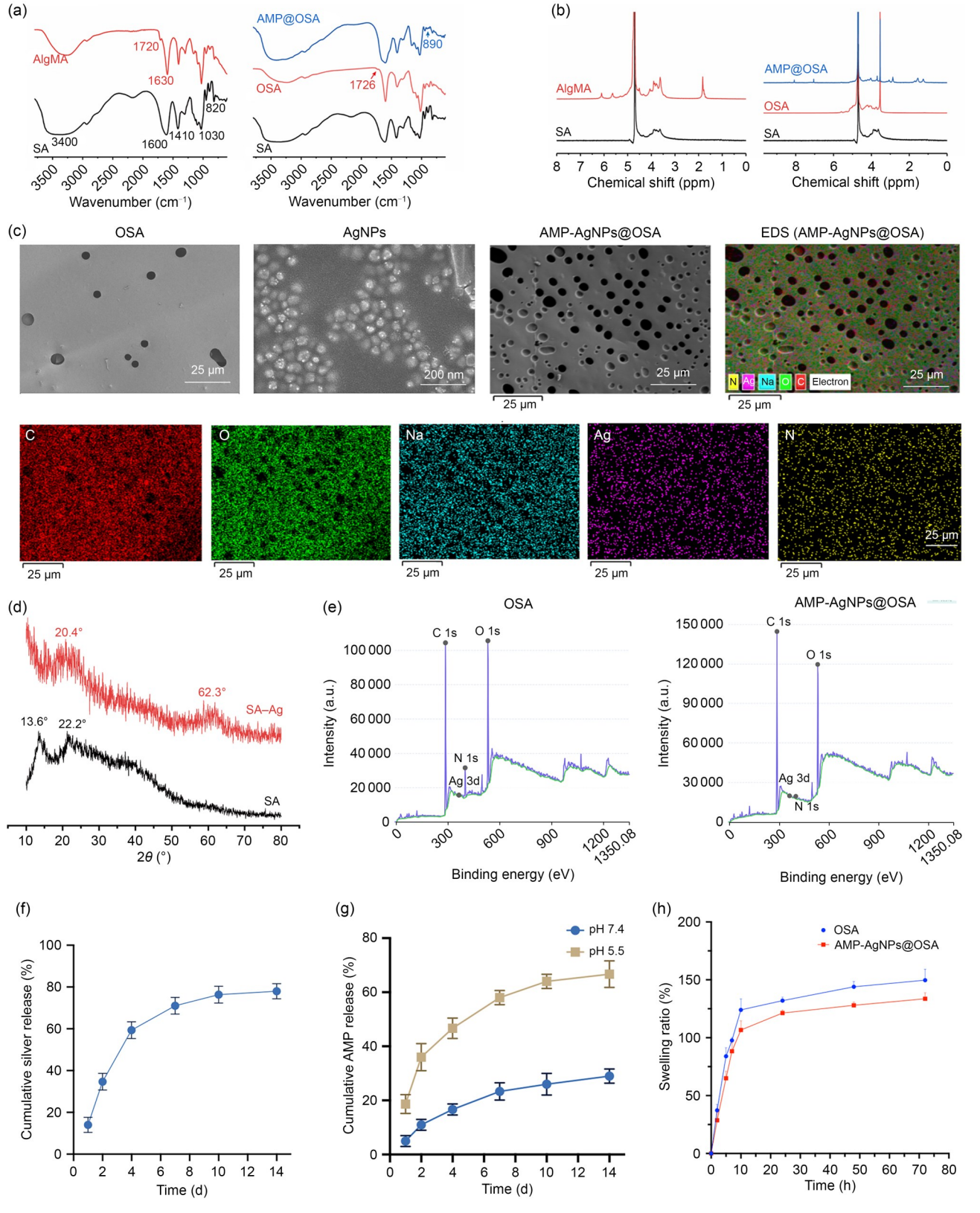

Fig. 2 Characterizations of AMP-AgNPs@OSA. (a) FTIR spectra. (b) NMR spectra. (c) SEM images of OSA, AgNPs, and AMP-AgNPs@OSA, and EDS mapping of AMP-AgNPs@OSA, showing element distributions of C, O, Na, Ag, and N. (d) XRD patterns of SA and SA–Ag, confirming AgNP crystallinity. (e) XPS spectra of the AMP-AgNPs@OSA hydrogel, confirming elemental composition. (f) Cumulative silver ion (Ag^+) release over time. (g) pH-responsive AMP release (faster at pH 5.5). (h) Swelling behavior of OSA and AMP-AgNPs@OSA hydrogels over time. Data are presented as mean±standard deviation (n=3). ppm: parts per million, equivalent to 10^{-6}

dual release system ensures both immediate and sustained antimicrobial activity, addressing acute infection control and prolonged microbial suppression. Figure 2h shows the swelling behavior of pure OSA and AMP-AgNPs@OSA hydrogels over 72 h. Both displayed rapid initial swelling, reaching equilibrium within 12 h. Incorporation of AMP-AgNPs slightly reduced equilibrium swelling (approximately 130%) compared with pure OSA (approximately 150%), reflecting enhanced structural stability from nanoparticle–peptide integration. Such controlled swelling maintains optimal moisture levels, promoting wound healing while preventing excessive structural deformation.

Figure 3a shows the sol–gel transition and photocuring behavior of the AMP-AgNPs@OSA hydrogel. The hydrogel exhibited a fluid state before UV exposure and rapidly transitioned into a stable gel upon curing. Compared with OSA, the AMP-AgNPs@OSA hydrogel showed enhanced gelation and excellent injectability, forming uniform droplets that solidified into predefined patterns under UV light while maintaining structural integrity (Fig. 3b). These characteristics confirm its reliable photocuring performance, making it suitable for biomedical applications requiring localized gelation.

Grafting AMPs onto OSA via Schiff base reactions and embedding AgNPs improved both hydrophilicity and functional performance (Figs. 3c and 3d). The static contact angle decreased from 73° to 53°, indicating enhanced wettability due to the introduction of polar groups from AMPs and uniform AgNP distribution. This modification exposed more hydrophilic segments, improved water interaction, and increased biocompatibility. Enhanced hydrophilicity facilitated AMP release, while AgNPs added synergistic antibacterial effects, making the hydrogel ideal for wound-healing and antibacterial applications. As shown in Figs. 3f and 3e, both the storage modulus (G') and loss modulus (G'') increased with increasing oscillation frequency. Compared with OSA, AMP-AgNPs@OSA exhibited higher G' and G'' values, indicating enhanced viscoelasticity after incorporation of AMP and AgNPs.

Thermal analysis (Figs. 3g and 3h) demonstrated that AMP-AgNPs@OSA possessed a higher degradation temperature and superior thermal stability than OSA, suggesting enhanced material robustness from nanoparticle incorporation. Crystallinity analysis (Fig. 3i) further showed that AMP-AgNPs@OSA possesses a more ordered structure, contributing to improved mechanical and thermal performance. The degradation profile (Fig. 3j) revealed a slower degradation rate for AMP-AgNPs@OSA than OSA, indicating prolonged functional effectiveness during wound healing. Collectively, these findings demonstrate that AMP-AgNPs@OSA hydrogel exhibits superior mechanical strength, swelling capacity, thermal stability, and controlled degradation, making it a strong candidate for skin wound-healing applications.

3.3 Antibacterial and anti-biofilm activity

The AMP-AgNPs@OSA hydrogel showed significantly fewer *S. aureus* and *E. coli* colonies than both the control and OSA-only groups ($p<0.05$; Figs. 4a and 4b), confirming its superior antibacterial efficacy. The AMPs likely disrupted bacterial membranes through electrostatic interactions, whereas AgNPs inhibited growth by releasing silver ions and generating reactive oxygen species (ROS). This dual mechanism markedly reduced bacterial viability on agar plates. Crystal violet staining (Figs. 4c and 4d) showed that AMP-AgNPs@OSA also suppressed biofilm formation more effectively than the control or OSA group. Biofilms formed by *S. aureus* and *E. coli* are typically resistant due to their protective extracellular polymeric matrix that impedes the diffusion of antimicrobial agents, making biofilm removal crucial for treating infected skin defects [25]. However, the integrated AMP-AgNPs system appeared to disrupt biofilm formation, likely by preventing bacterial adhesion at an early stage and interfering with intercellular signaling required for biofilm maturation. Confocal laser scanning microscopy (CLSM) images confirmed these effects (Figs. 4e and 4f). AMP-AgNPs@OSA-treated samples showed predominantly lower-intensity green fluorescence (live cells) and increased red fluorescence (dead cells), indicating strong bactericidal activity against established biofilms. The incorporation of AMP and AgNPs within an OSA carrier provided sustained antibacterial activity and a stable interface that suppressed bacterial colonization. The synergy between AMP membrane disruption and AgNP ion release with ROS generation enhanced inhibition. Furthermore, the hydrogel's pH-responsive AMP release ensured targeted antimicrobial activity in acidic, infected environments, minimizing cytotoxicity while maximizing bacterial eradication. The persistent antibacterial activity highlights its suitability for long-term infection control. Clinically, specific antimicrobial peptides could be selected based on bacterial susceptibility at wound sites and grafted onto the hydrogel for tailored, potent antibacterial effects. This multifunctional approach holds strong potential for preventing and managing biofilm-related infections in diverse biomedical applications.

3.4 Biocompatibility evaluation of AMP-AgNPs@OSA hydrogel

To assess the suitability of AMP-AgNPs@OSA hydrogel for treating infected wounds, we first assessed its cellular and blood compatibility. For in vitro cytotoxicity, NIH/3T3 fibroblasts were cultured with extracts of OSA and AMP-AgNPs@OSA hydrogels for 48 and 96 h. Live/Dead staining revealed a high proportion of viable cells in both hydrogel groups, indicating minimal cytotoxicity. Quantitative

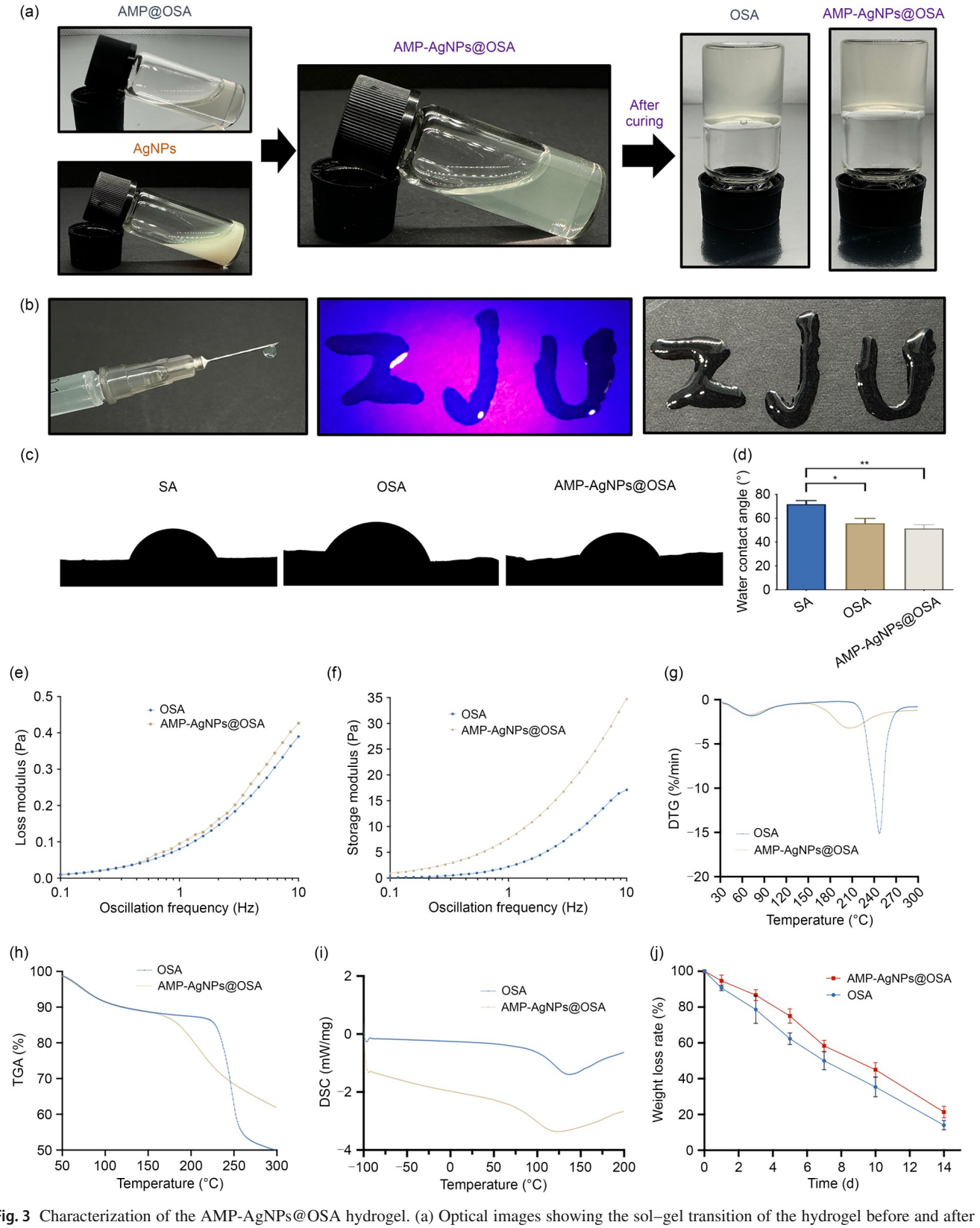

Fig. 3 Characterization of the AMP-AgNPs@OSA hydrogel. (a) Optical images showing the sol–gel transition of the hydrogel before and after UV curing. (b) Injectability and shape adaptability of the hydrogel under UV exposure. (c) Contact angle measurements of SA, OSA, and AMP-AgNPs@OSA, indicating hydrophilicity changes. (d) Quantification of water contact angles. (e, f) Loss modulus and storage modulus of OSA and AMP-AgNPs@OSA. (g–i) Thermal stability (DTG, TGA, and DSC). (j) Hydrogel degradation profile over 14 d. Data are presented as mean±standard deviation (n=3). $^{*}p< 0.05$ and $^{**}p<0.01$. DTG: derivative thermogravimetry

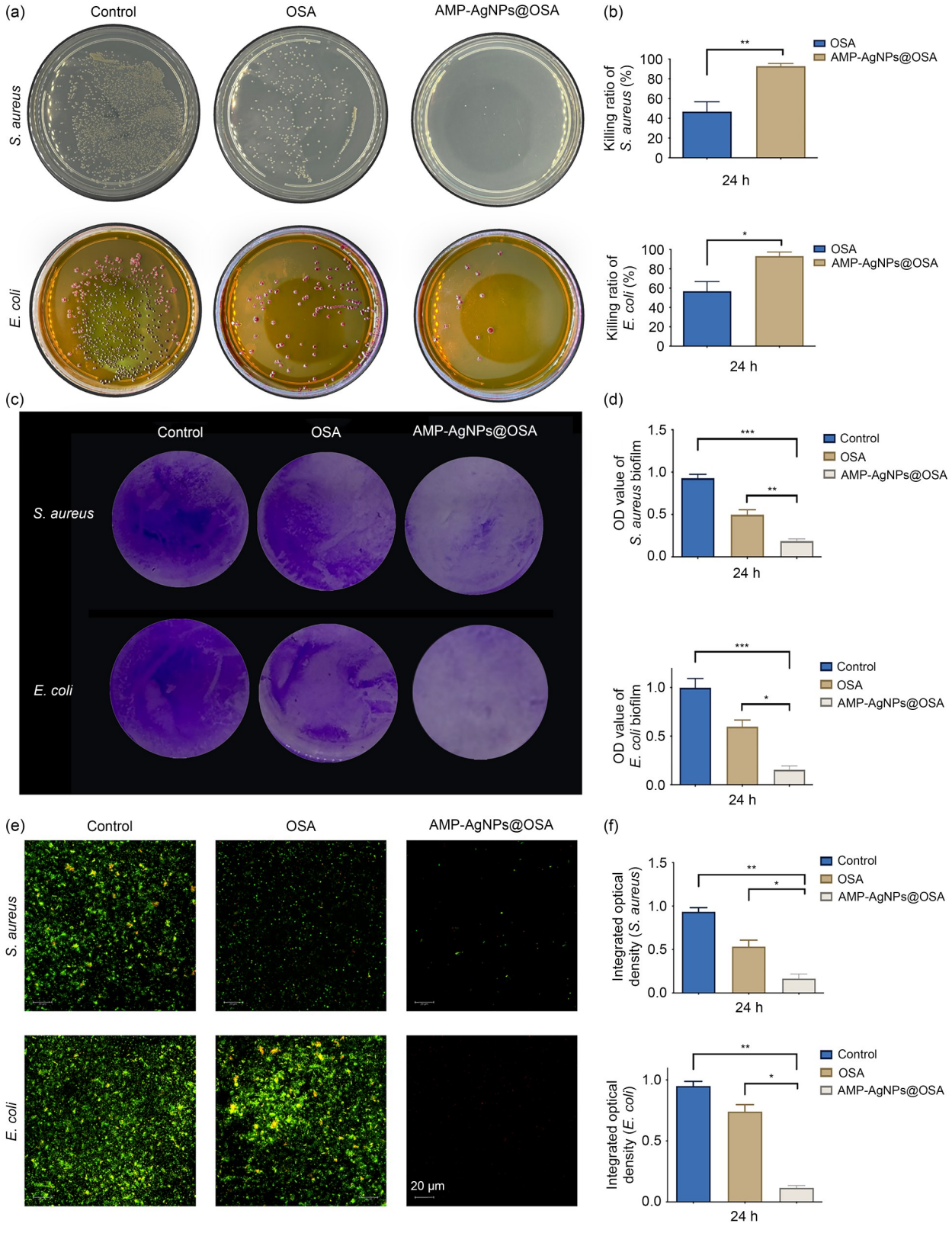

Fig. 4 Antibacterial and anti-biofilm performance of AMP-AgNPs@OSA against *S. aureus* and *E. coli*. (a) Representative agar plate images showing colony formation in the control, OSA, and AMP-AgNPs@OSA groups. (b) Quantitative analysis of colony counts. (c) Crystal violet staining of biofilms formed by *S. aureus* and *E. coli* in each group. (d) Biofilm quantification by absorbance measurements. (e) Confocal laser scanning microscopy images of live (green)/dead (red) staining in biofilms. (f) Quantification of live/dead fluorescence ratios. Data are presented as mean±standard deviation (n=3). $^{*}p<0.05$, $^{**}p<0.01$, and $^{***}p<0.001$. OD: optical density

proliferation assays corroborated these findings, showing comparable cell proliferation rates between hydrogel-exposed and control groups after 48 h (Figs. 5a and 5b). These results confirm that neither OSA nor AMP-AgNPs@OSA hydrogel extracts adversely affected fibroblast viability or growth, demonstrating favorable cytocompatibility.

Given the clinical importance of blood compatibility for wound dressings, a hemolysis assay was performed using PBS as the negative control and 0.1% Triton X-100 as the positive control. Hemolysis levels were quantified spectrophotometrically, with the positive control defined as 100% hemolysis. Both OSA and AMP-AgNPs@OSA hydrogels exhibited hemolysis rates below 2% across extract concentrations (Fig. 5c), confirming excellent blood compatibility well within the accepted threshold for materials in direct blood or tissue contact, highlighting the safety profile of the hydrogels.

The AMP-AgNPs@OSA hydrogel is composed mainly of OSA, AlgMA, AMPs, and AgNPs. Upon degradation, alginate components yield low-molecular-weight oligosaccharides or methacrylate fragments—biocompatible products known to support tissue repair [26]. AMPs degrade into amino acids or short peptides that are readily metabolized by the body without long-term toxicity [27]. The primary component warranting close monitoring is AgNPs, as high systemic doses can elicit acute toxicity. However, multiple studies indicate negligible chronic toxicity at low, clinically relevant levels [28]. In this formulation, AgNPs are topically

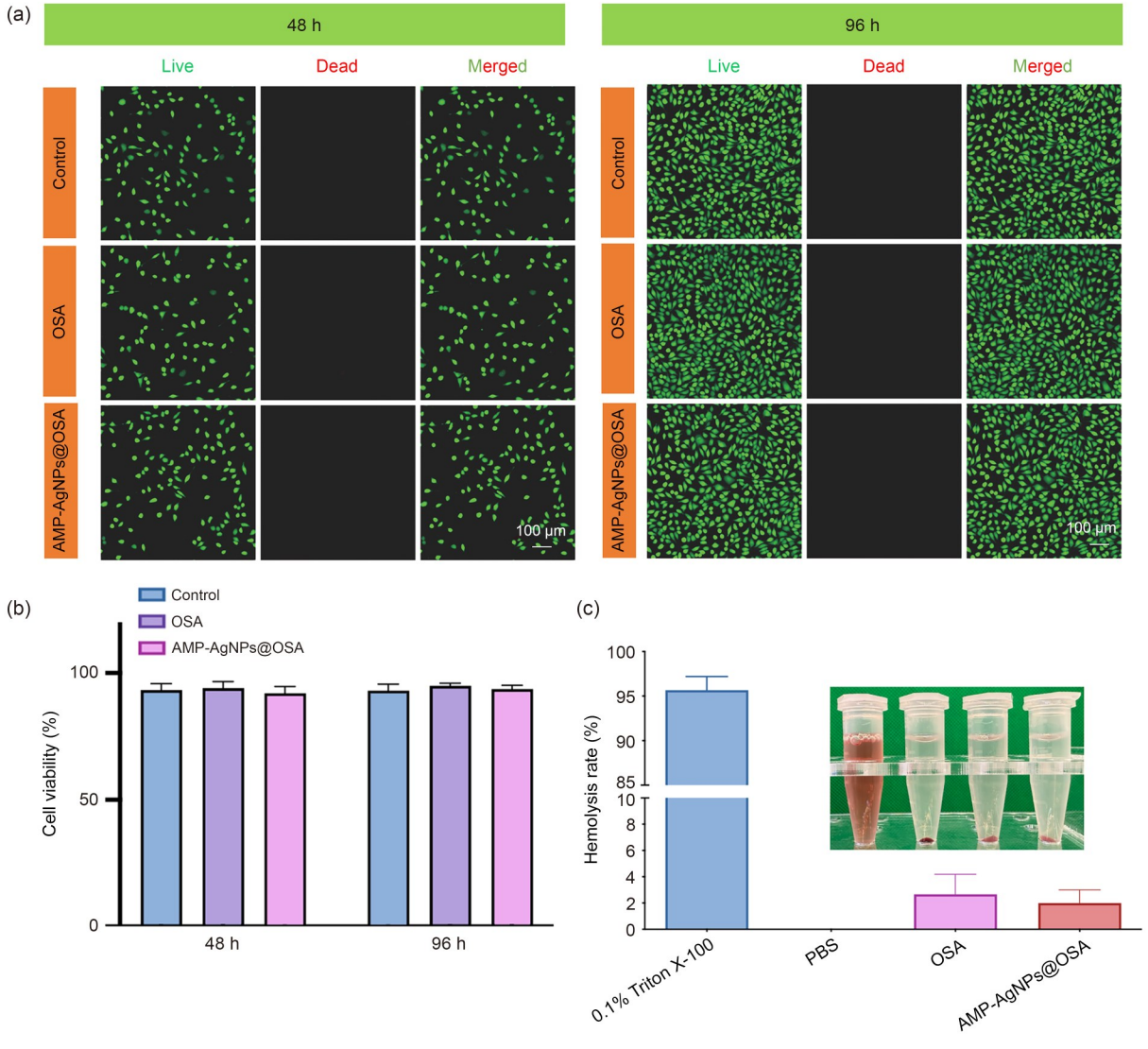

Fig. 5 Biocompatibility evaluation of the AMP-AgNPs@OSA hydrogel. (a) Live/Dead staining of NIH/3T3 cells cultured with different hydrogels (Control, OSA, and AMP-AgNPs@OSA) at 48 h and 96 h. Live cells are stained green, whereas dead cells are stained red. Scale bars: 100 μm. (b) Cell viability assay showing no significant cytotoxicity of the AMP-AgNPs@OSA hydrogel after 48 h and 96 h of incubation. (c) Hemolysis assay demonstrating the hemocompatibility of the AMP-AgNPs@OSA hydrogel compared with PBS and a positive control (0.1% Triton X-100). Inset: corresponding hemolysis test images. Data are presented as mean±standard deviation (n=3)

delivered within an alginate-based hydrogel, minimizing systemic uptake through matrix binding, local sequestration at the wound bed, and Ag^+ complexation with exudate proteins—collectively reducing bioavailable Ag^+ fraction relative to injectable dosing. These factors indicate that the AgNP concentration used remains within a conservative safety margin, supporting its clinical relevance for localized antimicrobial therapy in infected skin defects without incurring appreciable long-term systemic burden. Consistent with this rationale, our biocompatibility testing further confirmed that OSA-based hydrogels exhibited no significant cytotoxicity toward fibroblasts in vitro and caused minimal hemolytic activity, suggesting localized release without systemic toxicity. Moreover, the alginate matrix provides a biocompatible scaffold conducive to cell adhesion and proliferation. These properties are critical in wound dressings, in which balancing antimicrobial efficacy with tissue compatibility is essential. Demonstrating both low cytotoxicity and excellent hemocompatibility, the AMP-AgNPs@OSA hydrogel shows strong clinical potential for effectively controlling infection while preserving the integrity of surrounding tissues and blood components.

3.5 Transcriptomic insight into the immunomodulatory effects of AMP-AgNPs@OSA hydrogel

Transcriptome sequencing of NIH/3T3 fibroblasts was conducted to investigate the molecular mechanisms underlying the biological effects of AMP-AgNPs@OSA. The volcano plot (Fig. 6a) comparing the AMP-AgNPs@OSA and control groups revealed numerous DEGs. Significantly upregulated genes in the AMP-AgNPs@OSA group appear in red, whereas downregulated ones in blue, indicating a substantial transcriptional shift induced by the hydrogel. KEGG enrichment analysis (Fig. 6b) identified key pathways related to oxidative stress response and inflammatory regulation, aligning with the hydrogel's dual antimicrobial and immunomodulation functions. The heatmap (Fig. 6c) further highlighted distinct gene expression patterns induced by AMP-AgNPs@OSA, with clusters of genes involved in antioxidant defense and tissue repair being upregulated, whereas pro-inflammatory and tissue-damaging genes were suppressed compared with the control group. These findings suggest that the hydrogel promotes a cellular environment favoring reduced oxidative injury and enhanced tissue regeneration.

The Nrf2 and NF-κB pathways play opposing but interrelated roles in infected skin defects [29]. Nrf2 induces cytoprotective gene expression, mitigates oxidative stress, and supports tissue repair [30], whereas NF-κB activation triggers pro-inflammatory cytokine release that can exacerbate tissue damage if excessive [31]. Thus, coordinated modulation of these pathways—activating Nrf2 while suppressing overactive NF-κB—is critical for reducing inflammation, promoting M2 macrophage polarization, and accelerating skin healing, making them critical targets for treating infected skin wounds [32]. Gene set enrichment analysis (GSEA) showed positive enrichment of the Nrf2 signaling and related antioxidant pathways in cells treated with AMP-AgNPs@OSA (Fig. 6d), indicating enhanced cytoprotective gene expression. Currently, NF-κB-related inflammatory pathways are negatively enriched, reflecting a broad immunomodulatory response. Collectively, these transcriptomic results demonstrate that AMP-AgNPs@OSA hydrogel modulates cellular stress and inflammatory networks, fostering an environment conducive to wound healing and inflammation resolution.

HO-1, Nrf2, p65, and IκBα are critical regulators of the Nrf2 and NF-κB pathways, which play central roles in infected skin defect repair [33]. Nrf2, a transcription factor, activates antioxidant and cytoprotective genes, including HO-1, which mitigates oxidative stress, reduces inflammation, and promotes tissue regeneration [34]. Conversely, p65, a core NF-κB subunit, drives inflammation by inducing pro-inflammatory cytokines, exacerbating tissue damage, whereas IκBα inhibits NF-κB activation by sequestering p65 in the cytoplasm; its degradation leads to NF-κB activation and inflammation [35]. The interplay of these molecules governs macrophage polarization: Nrf2/HO-1 activation promotes M2 macrophages with anti-inflammatory and regenerative effects, whereas NF-κB activation skews macrophages toward the pro-inflammatory M1 phenotype. Balancing these pathways is thus vital for reducing inflammation, enhancing collagen deposition, and promoting vascularization during wound healing. Western blotting (Fig. 6e) provided mechanistic confirmation of transcriptomic findings, showing that AMP-AgNPs@OSA treatment upregulated HO-1 and Nrf2—key antioxidant mediators—while downregulating p65 and IκBα, thereby decreasing NF-κB activity. Quantitative data (Fig. 6f) corroborated these results, with HO-1 and Nrf2 levels significantly increased and p65 levels markedly reduced ($p<0.05$). Collectively, these molecular shifts indicate that AMP-AgNPs@OSA operates via a dual mechanism: activating Nrf2-dependent antioxidant defenses while suppressing NF-κB-driven inflammation.

These results highlight the capacity of AMP-AgNPs@OSA to induce coordinated transcriptional and translational changes that strengthen cellular stress resistance and suppress inflammatory signaling. By upregulating Nrf2-HO-1 and inhibiting NF-κB, the hydrogel establishes a microenvironment favorable for tissue repair and infection control—an essential balance for wound-healing applications, where excessive oxidative stress and persistent inflammation often impede regeneration. Overall, the transcriptomic and protein-level data support AMP-AgNPs@OSA as a multifunctional biomaterial capable of synergizing antimicrobial efficacy with robust immunomodulatory and cytoprotective functions.

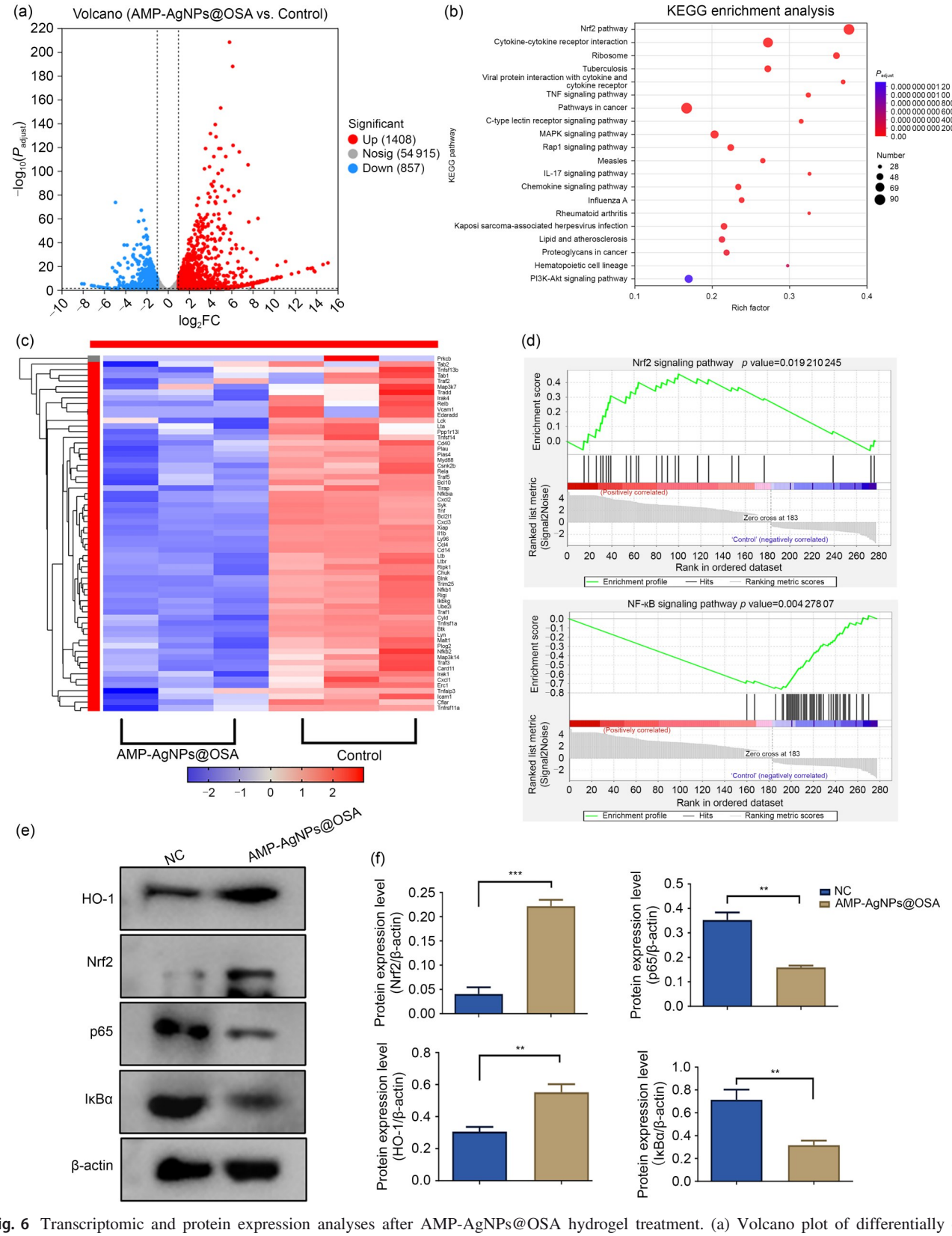

Fig. 6 Transcriptomic and protein expression analyses after AMP-AgNPs@OSA hydrogel treatment. (a) Volcano plot of differentially expressed genes between the AMP-AgNPs@OSA and control groups. (b) KEGG pathway enrichment identifying activated signaling pathways. (c) Heatmap of differentially expressed genes (upregulated in red, downregulated in blue). (d) GSEA showing activation and inhibition of the Nrf2 and NF-κB signaling pathways, respectively. (e) Western blotting of HO-1, Nrf2, p65, and IκBα expression levels. (f) Quantification of protein expression levels. Data are presented as mean±standard deviation (n=3). $^{**}p$<0.01 and $^{***}p$<0.001. NC: negative control

3.6 Macrophage polarization and immune modulation

Macrophages play a crucial role in wound healing through dynamic M1/M2 polarization [36]. Pro-inflammatory M1 macrophages combat infection in the early stages by releasing cytokines such as tumor necrosis factor-α (TNF-α) and IL-1β but can impair healing if overactivated. In contrast, M2 macrophages promote tissue repair by secreting anti-inflammatory cytokines such as IL-10 and transforming growth factor-β (TGF-β), facilitating collagen synthesis and angiogenesis [37]. Effective wound repair requires a timely transition from M1 to M2 polarization [38]. Photocurable biomaterials enhance this immunomodulation by providing spatiotemporal control over local microenvironments, decreasing NF-κB-mediated cytokine cascades while promoting M2-associated repair [39]. To evaluate the immunoregulatory effects of AMP-AgNPs@OSA, macrophage polarization was analyzed via immunofluorescence staining, flow cytometry, and Western blotting. The results demonstrated that the hydrogel effectively promoted M1 to M2 polarization, suggesting its role in inflammation regulation and tissue regeneration. As shown in Figs. 7a and 7b, IL-4 treatment increased the M2 marker CD206 expression, whereas LPS induced the M1 marker inducible nitric oxide synthase (iNOS). The OSA group exhibited moderate modulation, whereas the AMP-AgNPs@OSA group markedly enhanced CD206 expression and reduced iNOS expression. Quantitative fluorescence confirmed significantly higher CD206 intensity and suppressed iNOS expression in the AMP-AgNPs@OSA group compared with the OSA and LPS groups ($p<0.05$; Fig. 7c), indicating that AMP-AgNPs@OSA hydrogel effectively facilitated macrophage polarization toward the M2 phenotype and attenuated M1-mediated inflammation. Flow cytometry further demonstrated the phenotypic shifts in macrophage populations under different treatment conditions (Fig. 7d). The IL-4-treated group exhibited a substantial increase in the proportion of $CD206^+$ macrophages, whereas LPS treatment resulted in a predominance of $CD86^+$ macrophages, indicative of M1 polarization. Notably, the AMP-AgNPs@OSA group demonstrated a significantly higher percentage of $CD206^+$ cells and a lower percentage of $CD86^+$ cells compared with the OSA group, closely resembling the IL-4-induced M2 polarization pattern (Fig. 7e). These results suggest that AMP-AgNPs@OSA hydrogel both reduced pro-inflammatory macrophage accumulation and increased the formation of reparative macrophages, thereby contributing to a favorable immune microenvironment for tissue regeneration. Western blotting results (Figs. 7f and 7g) validated these findings, showing downregulation of M1 markers CD86 and iNOS, alongside upregulation of M2-associated proteins Arg-1 and CD206, further confirming that the AMP-AgNPs@OSA hydrogel effectively suppresses M1-driven inflammation and promotes M2-mediated tissue repair.

These immunoregulatory outcomes align with the transcriptomic data. First, the incorporation of AMPs and AgNPs conferred potent antibacterial activity, lowering pathogen burden and reducing M1-promoting inflammation [40]. Second, the bioactive hydrogel microenvironment activates signaling pathways such as Nrf2 to enhance M2 polarization [41]. Additionally, its pH-responsive nature allows controlled AMP release under acidic conditions, enabling infection control while maintaining immune equilibrium. This controlled release is crucial for preventing excessive immune activation and fostering efficient tissue repair.

3.7 Enhanced wound healing and immunomodulatory effects of AMP-AgNPs@OSA hydrogel

The wound closure process was monitored over 12 d to evaluate the healing efficacy of the AMP-AgNPs@OSA hydrogel in an infected full-thickness skin defect model. Figure 8 depicts the progression of wound healing and bacterial clearance in a rat model of *S. aureus*-infected skin defects treated with the AMP-AgNPs@OSA hydrogel. As shown in Fig. 8a, infection and treatment were initiated on Day 0, with observations and histological analyses performed on Day 12. Representative images in Fig. 8b illustrate accelerated wound healing at different time points (Days 0, 2, 5, 7, 10, and 12) in the AMP-AgNPs@OSA group compared with the control and OSA groups. Although the OSA hydrogel group enhanced wound healing compared with the control group, the AMP-AgNPs@OSA group achieved the most significant wound size reduction by Day 12, confirming superior healing performance.

Quantitative analysis (Fig. 8c) demonstrated significantly faster wound closure in the AMP-AgNPs@OSA group at Days 5, 7, 10, and 12 compared with the control and OSA groups ($p<0.05$). Wound trace maps, as shown in Fig. 8d, further confirmed reduced wound size in the AMP-AgNPs@OSA group over time. The color-coded circles represent wound size at each time point, with the AMP-AgNPs@OSA group showing the smallest residual wound area by Day 12. Body weight data (Fig. 8e) revealed no significant intergroup differences, indicating that treatment did not compromise systemic health, thereby supporting the in vivo biocompatibility of both the hydrogel and AgNP degradation products. Bacteria quantification (Fig. 8f) showed a more significant reduction in *S. aureus* load at Days 2 and 7 in the AMP-AgNPs@OSA group than in the control and OSA groups ($p<0.05$), demonstrating the hydrogel's effective antibacterial properties.

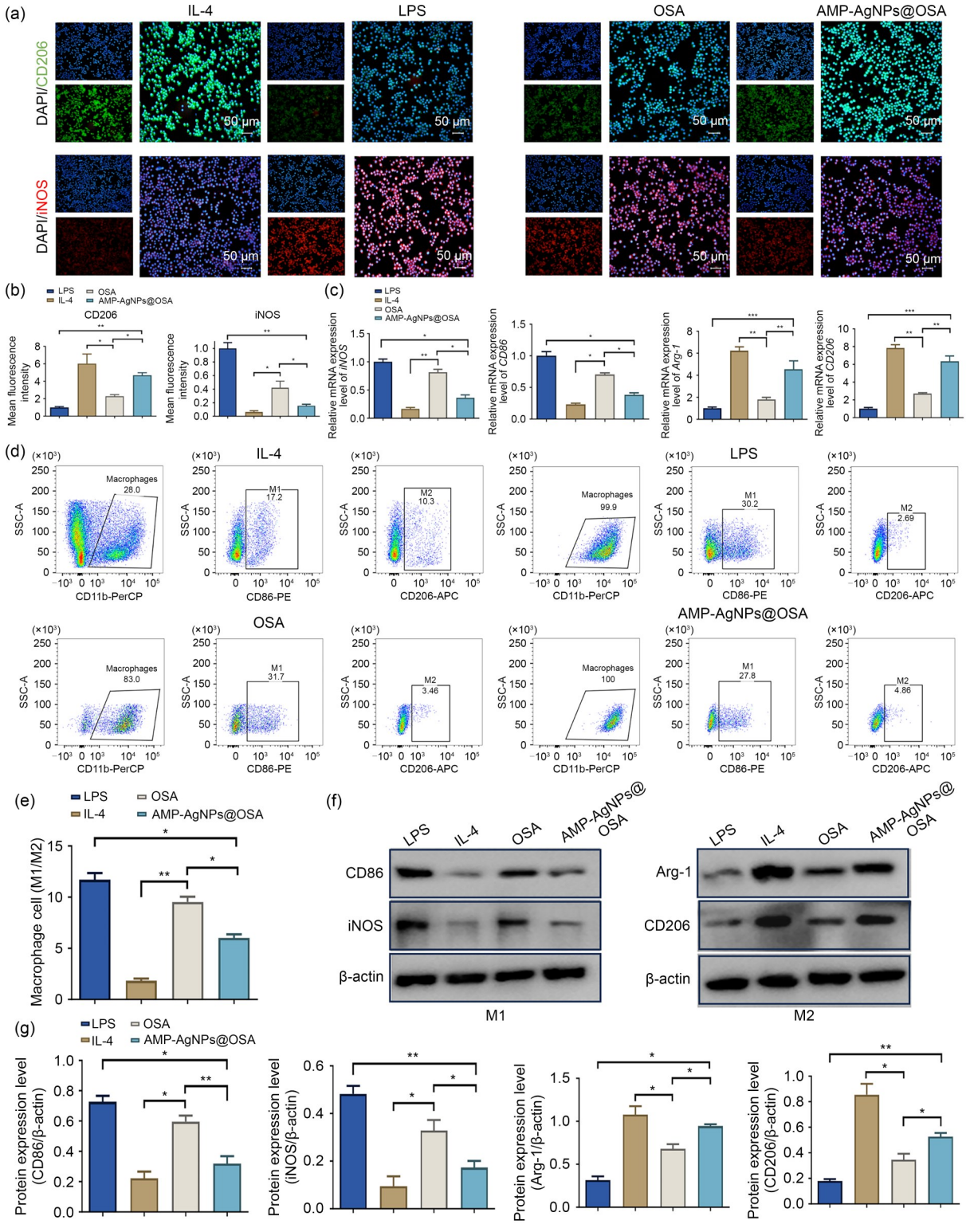

Fig. 7 Immunomodulatory effects of the AMP-AgNPs@OSA hydrogel on macrophage polarization. (a) Immunofluorescence staining of CD206 (M2 marker, green) and iNOS (M1 marker, red) in macrophages treated with IL-4, LPS, OSA hydrogel, or AMP-AgNPs@OSA hydrogel. Nuclei were stained with DAPI (blue). Scale bars: 50 μm. (b) Quantification of CD206 and iNOS fluorescence intensity across treatment groups. (c) Relative mRNA expression levels of *iNOS*, *CD86*, *Arg-1*, and *CD206* in macrophages under different treatments. (d) Flow cytometry analysis of macrophages labeled with CD86 (M1 marker) and CD206 (M2 marker) under different conditions. (e) M1/M2 macrophage ratio derived from flow cytometry. (f) Western blotting of M1 (CD86, iNOS) and M2 (Arg-1, CD206) macrophage markers in different groups. β-actin served as the loading control. (g) Quantification of relative protein expression levels of CD86, iNOS, Arg-1, and CD206 from Western blotting results. Data are presented as mean±standard deviation (n=3). $^{*}p<0.05$, $^{**}p<0.01$, and $^{***}p<0.001$

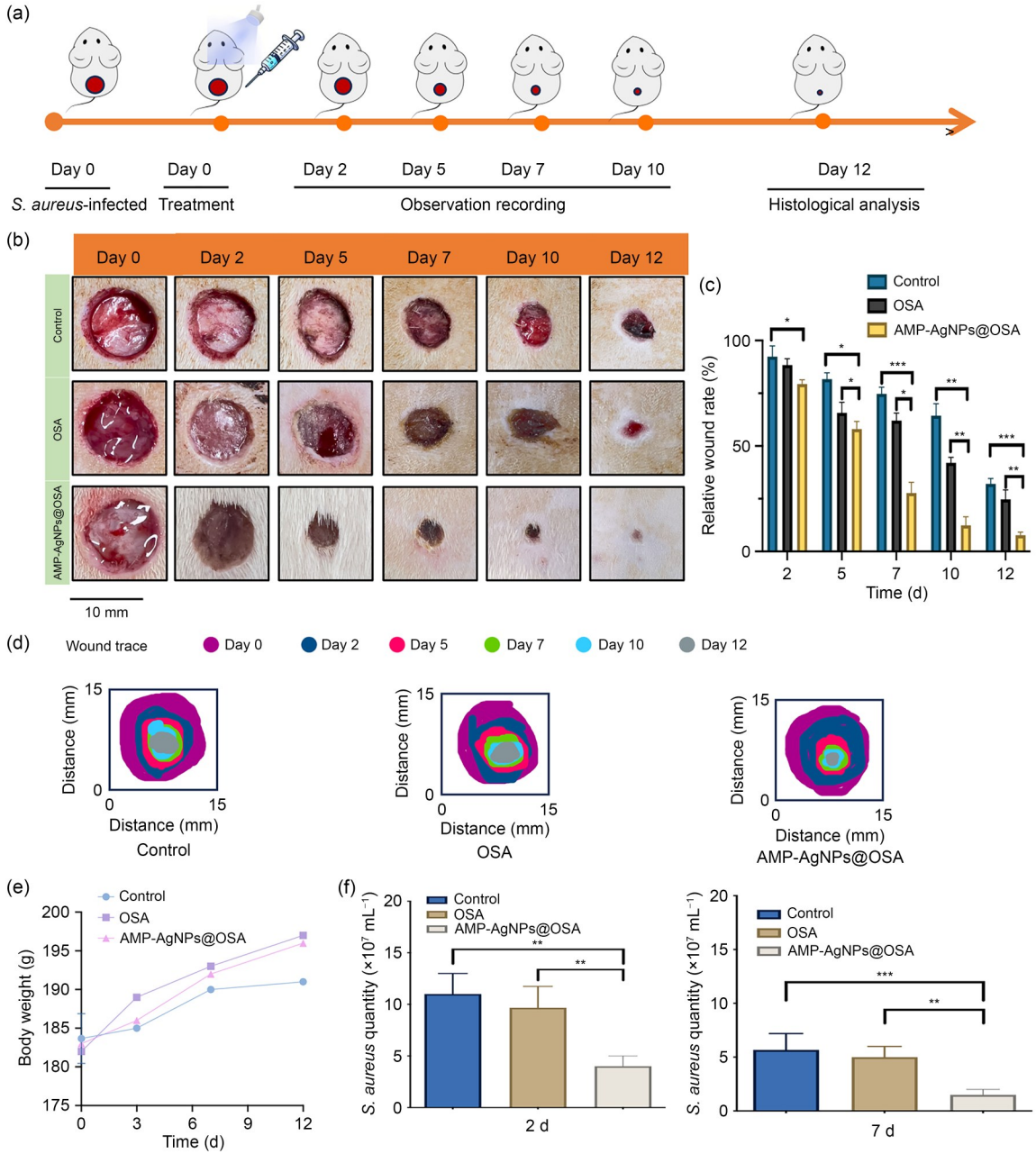

Fig. 8 Evaluation of wound healing and bacterial clearance in an infected skin defect model treated with the AMP-AgNPs@OSA hydrogel. (a) Schematic of the experimental timeline for *S. aureus*-infected wound treatment. (b) Representative images of wound healing progression in the different groups (Control, OSA, and AMP-AgNPs@OSA) at Days 0, 2, 5, 7, 10, and 12. Scale bar: 10 mm. (c) Quantification of the relative wound rate over time. (d) Wound trace maps showing wound size reduction across groups. (e) Body weight changes throughout the study. (f) Quantification of *S. aureus* bacterial load in wound tissue at Days 2 and 7 using RT-PCR. Data are presented as mean±standard deviation (n=3). $^{*}p<0.05$, $^{**}p<0.01$, and $^{***}p<0.001$

The enhanced wound healing efficacy of the AMP-AgNPs@OSA hydrogel can be attributed to its multifunctional design. Its pH-responsive release of AMP effectively suppressed *S. aureus* proliferation, mitigating infection and inflammation at the wound site. Additionally, AgNPs exerted broad-spectrum antibacterial effects, further preventing secondary infection. The hydrogel's Schiff base-crosslinked double-network structure maintained mechanical stability and a moist wound environment—conditions essential for tissue regeneration.

Immunomodulation also contributed significantly to wound healing. Previous studies have shown that macrophage polarization toward the M2 phenotype is critical for tissue repair [42]. The AMP-AgNPs@OSA hydrogel promoted M2 polarization, thereby reducing inflammation and accelerating tissue regeneration. Its bioactive matrix likely enhanced

extracellular matrix deposition, consistent with the accelerated re-epithelialization observed in the wound images. Histological and immunohistochemical analyses were further conducted to assess tissue regeneration and inflammatory responses in a rat dorsal wound model treated with OSA-based hydrogels. H&E, Masson's trichrome, and immunohistochemical staining for IL-10 and IL-6 were used to evaluate re-epithelialization, collagen deposition, and inflammatory modulation across control, OSA, and AMP-AgNPs@OSA groups. As shown in Fig. 9a, H&E staining revealed pronounced tissue regeneration and reduced inflammation in the AMP-AgNPs@OSA group; the OSA group showed moderate improvement compared with the control group. Figure 9b displays Masson's trichrome staining, which highlights greater collagen deposition in the AMP-AgNPs@OSA group, indicating enhanced wound

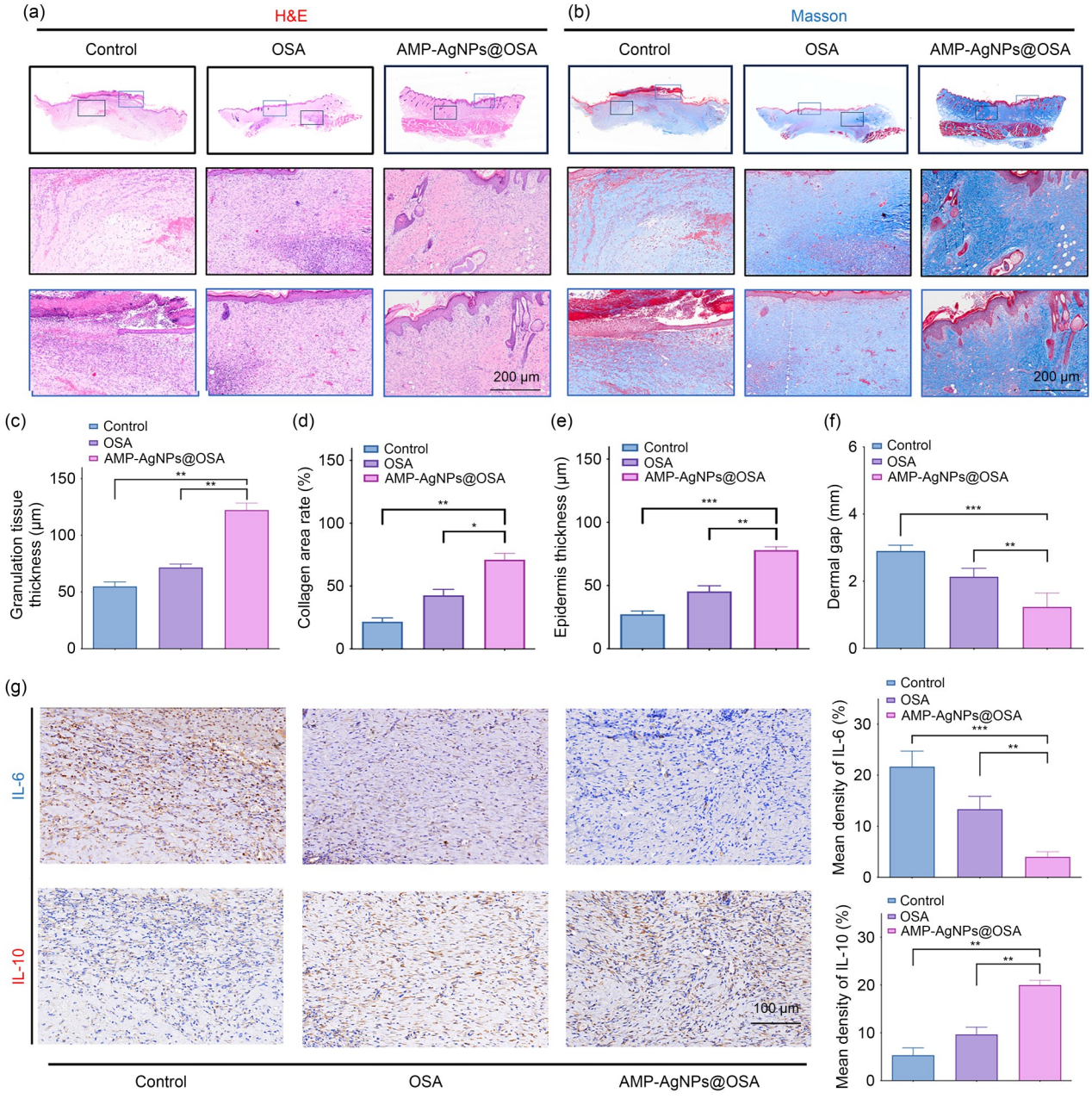

Fig. 9 Histological and immunohistochemical analysis of wound healing in the infected skin defect model. (a) H&E staining of wound sections from different treatment groups (Control, OSA, and AMP-AgNPs@OSA). Scale bar: 200 μm. (b) Masson's trichrome staining to assess collagen deposition in wound tissue. Scale bar: 200 μm. (c) Quantification of granulation tissue thickness among different groups. (d) Collagen matrix percentage in the different groups based on Masson staining. (e) Epidermal thickness assessment of healed skin. (f) Dermal gap measurements among groups, demonstrating wound closure efficiency. (g) Immunohistochemical staining and quantification of IL-6 and IL-10 in wound tissue to evaluate inflammatory responses. Scale bar: 100 μm. Data are presented as mean±standard deviation (n=3). $^{*}p<0.05$, $^{**}p<0.01$, and $^{***}p<0.001$

healing and tissue repair. Quantitative analysis (Figs. 9c and 9d) confirmed a significantly higher thickness and collagen area percentage ($p<0.05$). Figure 9e shows that the AMP-AgNPs@OSA treatment produced a thicker epidermal layer than both comparison groups, while Fig. 9f illustrates a smaller dermal gap, confirming improved wound closure. Immunohistochemical staining (Fig. 9g) showed that AMP-AgNPs@OSA treatment significantly reduced IL-6 and increased IL-10 expression compared with the control and OSA groups, further supporting a shift toward an anti-inflammatory milieu. Quantitative analysis corroborated these trends, highlighting the hydrogel's capacity to suppress inflammation while promoting tissue repair.

Collectively, these results demonstrate that the AMP-AgNPs@OSA hydrogel enhanced fibroblast activity and accelerated dermal remodeling, which is crucial for stable wound healing. IL-10 and IL-6 are key cytokines involved in infected skin repair [43]. IL-10 exerts anti-inflammatory effects by suppressing pro-inflammatory cytokine production, promoting M2 macrophage polarization, and facilitating tissue regeneration [44]. In contrast, IL-6 plays a dual role: it recruits immune cells and supports early inflammation but may cause chronic inflammation if persistently elevated [45]. Thus, maintaining an appropriate IL-10/IL-6 balance is critical for modulating inflammation, promoting angiogenesis, and accelerating wound healing—making these cytokines important therapeutic targets. Immunohistochemical staining for IL-10 and IL-6 confirmed the hydrogel's immunomodulatory properties. Strong IL-6 staining in the control group indicated persistent inflammation while the OSA hydrogel group showed lower IL-6 and higher IL-10 expression, suggesting partial inflammation resolution. In the AMP-AgNPs@OSA group, IL-10 expression was significantly upregulated, whereas IL-6 expression was significantly downregulated, confirming an anti-inflammatory microenvironment. This immunomodulatory effect likely resulted from the synergistic actions of the AMPs and AgNPs, which suppress excessive immune activation and promote M2 macrophage polarization. However, further in vivo mechanistic studies are needed to verify whether the hydrogel directly induces macrophage polarization or activates the proposed signaling pathways. Further studies will also include commercially available wound dressings or other bioactive hydrogels as controls to better contextualize the immunomodulatory effects.

4 Conclusions

This study demonstrates the strong therapeutic potential of the light-curable AMP-AgNPs@OSA hydrogel—composed of OSA, AlgMA, AMPs, and AgNPs—for treating infected skin defects. The hydrogel exhibited broad-spectrum antibacterial activity and pH-responsive AMP release, enabling targeted antimicrobial action in acidic wound environments. It promoted M2 macrophage polarization, reduced inflammation, and accelerated tissue regeneration. In a rat dorsal wound infection model, AMP-AgNPs@OSA significantly reduced wound size compared with the control and OSA groups. Histological analyses revealed increased collagen deposition and extracellular matrix formation, while immunohistochemical staining showed lower IL-6 expression, reduced inflammatory cell infiltration, and elevated IL-10 levels. Collectively, these findings confirm the hydrogel's ability to suppress inflammation, promote angiogenesis, and enhance wound healing. The AMP-AgNPs@OSA hydrogel thus represents a multifunctional platform for managing infected skin wounds, integrating antibacterial, anti-inflammatory, and pro-regenerative properties. Furthermore, the AMP component can be replaced with clinically relevant antibiotics based on antimicrobial susceptibility testing, allowing personalized infection control. These results underscore the hydrogel's strong translational potential for advanced clinical applications in infected skin repair.

Supplementary Information The online version contains supplementary material available at https://doi.org/10.1631/bdm.2500380.

Acknowledgements This work was supported by the "Pioneer" and "Leading Goose" R&D Program of Zhejiang (No. 2025C02102) and the National Natural Science Foundation of China (No. 82471034).

Author contributions XLL: conceptualization, methodology, investigation, formal analysis, and writing—original draft. TF: methodology, investigation, validation, data curation, and writing—original draft. YQL: methodology, investigation, formal analysis, visualization, and writing—original draft. JJX: validation, formal analysis, and data curation. HHZ: conceptualization, resources, writing—review & editing, supervision, project administration, and funding acquisition. FDZ: conceptualization, resources, writing—review & editing, supervision, and funding acquisition.

Declarations

Conflict of interest The authors declare that they have no conflict of interest.

Ethical approval All the animal experiments were approved by the Zhejiang University Institutional Animal Care and Use Committee and conducted ethically according to the principles of the National Research Council's Guide for the Care and Use of Laboratory Animals (approval number: ZJU20241039).

Data availability The data supporting this study are available within the manuscript and its supplementary materials.

Use of generative AI tools No generative AI tools were used in the preparation of this manuscript.

References

1. Sorg H, Tilkorn DJ, Hager S et al (2017) Skin wound healing: an update on the current knowledge and concepts. *Eur Surg Res*

58(1–2):81–94.
https://doi.org/10.1159/000454919
2. Pignet AL, Hecker A, Voljc T et al (2024) The use of acellular fish skin grafts in burns and complex trauma wounds: a systematic review of clinical data. *Plast Aesthet Res* 11:40.
https://doi.org/10.20517/2347-9264.2024.54
3. Battaglia M, Ann GS (2023) *Staphylococcus xylosus* and *Staphylococcus aureus* as commensals and pathogens on murine skin. *Lab Anim Res* 39(1):18.
https://doi.org/10.1186/s42826-023-00169-0
4. Kavanagh F, Rozen W, Seth I et al (2024) Exploring the efficacy of negative pressure wound therapy in the management of mycobacterium ulcerans wounds: a comprehensive literature review. *Plast Aesthet Res* 11:43.
https://doi.org/10.20517/2347-9264.2024.26
5. Lei J, Sun L, Li P et al (2019) The wound dressings and their applications in wound healing and management. *Health Sci J* 13(4):662.
https://doi.org/10.21767/1791-809X.1000662
6. Wang WD, Ummartyotin S, Narain R (2023) Advances and challenges on hydrogels for wound dressing. *Curr Opin Biomed Eng* 26:100443.
https://doi.org/10.1016/j.cobme.2022.100443
7. Brumberg V, Astrelina T, Malivanova T et al (2021) Modern wound dressings: hydrogel dressings. *Biomedicines* 9(9):1235.
https://doi.org/10.3390/biomedicines9091235
8. Chen X, Zhang YH, Yu W et al (2023) In situ forming ROS-scavenging hybrid hydrogel loaded with polydopamine-modified fullerene nanocomposites for promoting skin wound healing. *J Nanobiotechnol* 21(1):129.
https://doi.org/10.1186/s12951-023-01879-2
9. Song YT, Hu QX, Liu SH et al (2024) Electrospinning drug-loaded polycaprolactone/polycaprolactone-gelatin multi-functional bilayer nanofibers composite scaffold for postoperative wound healing of cutaneous squamous cell carcinoma. *Biomed Technol* 8:65–80.
https://doi.org/10.1016/j.bmt.2024.10.001
10. Lin JN, Jiao GL, Kermanshahi-pour A (2022) Algal polysaccharides-based hydrogels: extraction, synthesis, characterization, and applications. *Mar Drugs* 20(5):306.
https://doi.org/10.3390/md20050306
11. Wang X, Yao XY, Sun ZY et al (2023) An extracellular matrix mimicking alginate hydrogel scaffold manipulates an inflammatory microenvironment and improves peripheral nerve regeneration by controlled melatonin release. *J Mater Chem B* 11(48):11552–11561.
https://doi.org/10.1039/d3tb01727c
12. Ji SQ, An FY, Zhang TW et al (2024) Antimicrobial peptides: an alternative to traditional antibiotics. *Eur J Med Chem* 265:116072.
https://doi.org/10.1016/j.ejmech.2023.116072
13. Kalwar K, Shan D (2018) Antimicrobial effect of silver nanoparticles (AgNPs) and their mechanism – a mini review. *Micro Nano Lett* 13(3):277–280.
https://doi.org/10.1049/mnl.2017.0648
14. Jahan I, Matpan Bekler F, Tunç A et al (2024) The effects of silver nanoparticles (AgNPs) on thermophilic bacteria: antibacterial, morphological, physiological and biochemical investigations. *Microorganisms* 12(2):402.
https://doi.org/10.3390/microorganisms12020402
15. Zhang YH, Kang J, Chen X et al (2023) Ag nanocomposite hydrogels with immune and regenerative microenvironment regulation promote scarless healing of infected wounds. *J Nanobiotechnol* 21(1):435.
https://doi.org/10.1186/s12951-023-02209-2
16. Zhang XQ, Yu W, Zhang YH et al (2024) A hydrogen generator composed of poly (lactic-co-glycolic acid) nanofibre membrane loaded iron nanoparticles for infectious diabetic wound repair. *J Colloid Interface Sci* 672:266–278.
https://doi.org/10.1016/j.jcis.2024.05.222
17. Gounden V, Singh M (2024) Hydrogels and wound healing: current and future prospects. *Gels* 10(1):43.
https://doi.org/10.3390/gels10010043
18. Farshidfar N, Iravani S, Varma RS (2023) Alginate-based biomaterials in tissue engineering and regenerative medicine. *Mar Drugs* 21(3):189.
https://doi.org/10.3390/md21030189
19. Zivari-Ghader T, Rashidi MR, Mehrali M (2024) Biological macromolecule-based hydrogels with antibacterial and antioxidant activities for wound dressing: a review. *Int J Biol Macromol* 279:134578.
https://doi.org/10.1016/j.ijbiomac.2024.134578
20. Gao C, Tang F, Gong GY et al (2017) PH-responsive prodrug nanoparticles based on a sodium alginate derivative for selective co-release of doxorubicin and curcumin into tumor cells. *Nanoscale* 9(34):12533–12542.
https://doi.org/10.1039/c7nr03611f
21. Weng WQ, Wang L, Fan L et al (2024) Ordered micro-nano structured biomaterials for wound healing. *Biomed Technol* 8:104–114.
https://doi.org/10.1016/j.bmt.2024.09.001
22. Kim SY, Nair MG (2019) Macrophages in wound healing: activation and plasticity. *Immunol Cell Biol* 97(3):258–267.
https://doi.org/10.1111/imcb.12236
23. Zhao Y, Li MX, Mao JY et al (2024) Immunomodulation of wound healing leading to efferocytosis. *Smart Med* 3(1):e20230036.
https://doi.org/10.1002/SMMD.20230036
24. Chen CJ, Lin ZM, Liu WB et al (2022) Emodin accelerates diabetic wound healing by promoting anti-inflammatory macrophage polarization. *Eur J Pharmacol* 936:175329.
https://doi.org/10.1016/j.ejphar.2022.175329
25. Shan JY, Che JY, Song CH et al (2023) Emerging antibacterial nanozymes for wound healing. *Smart Med* 2(3):e20220025.
https://doi.org/10.1002/SMMD.20220025
26. Wang MP, Chen L, Zhang ZJ (2021) Potential applications of alginate oligosaccharides for biomedicine – a mini review. *Carbohydr Polym* 271:118408.
https://doi.org/10.1016/j.carbpol.2021.118408
27. Ma XX, Aminov R, Franco OL et al (2024) Editorial: antimicrobial peptides and their druggability, bio-safety, stability, and resistance. *Front Microbiol* 15:1425952.
https://doi.org/10.3389/fmicb.2024.1425952
28. Kim YS, Song MY, Park JD et al (2010) Subchronic oral toxicity of silver nanoparticles. *Part Fibre Toxicol* 7(1):20.
https://doi.org/10.1186/1743-8977-7-20
29. Ambrozova N, Ulrichova J, Galandakova A (2017) Models for the study of skin wound healing. The role of Nrf2 and NF-κB. *Biomed Pap Med Fac Univ Palacky Olomouc Czech Repub* 161(1):1–13.
https://doi.org/10.5507/bp.2016.063
30. Vallion R, Kerdine-Römer S (2022) Regulation of the immune response to contact sensitizers by Nrf2. *Contact Dermatitis* 87(1):13–19.
https://doi.org/10.1111/cod.14073

31. Saha S, Buttari B, Panieri E et al (2020) An overview of Nrf2 signaling pathway and its role in inflammation. *Molecules* 25(22): 5474.
https://doi.org/10.3390/molecules25225474
32. Wang N, Liang HW, Zen K (2014) Molecular mechanisms that influence the macrophage M1-M2 polarization balance. *Front Immunol* 5:614.
https://doi.org/10.3389/fimmu.2014.00614
33. Lv HM, Ren WZ, Zheng YW et al (2016) Tenuigenin exhibits anti-inflammatory activity via inhibiting MAPK and NF-κB and inducing Nrf2/HO-1 signaling in macrophages. *Food Funct* 7(1): 355–363.
https://doi.org/10.1039/c5fo00807g
34. Loboda A, Damulewicz M, Pyza E et al (2016) Role of Nrf2/HO-1 system in development, oxidative stress response and diseases: an evolutionarily conserved mechanism. *Cell Mol Life Sci* 73(17):3221–3247.
https://doi.org/10.1007/s00018-016-2223-0
35. Li QT, Verma IM (2002) NF-κB regulation in the immune system. *Nat Rev Immunol* 2(10):725–734.
https://doi.org/10.1038/nri910
36. Mao JY, Chen L, Cai ZW et al (2022) Advanced biomaterials for regulating polarization of macrophages in wound healing. *Adv Funct Mater* 32(12):2111003.
https://doi.org/10.1002/adfm.202111003
37. Shapouri-Moghaddam A, Mohammadian S, Vazini H et al (2018) Macrophage plasticity, polarization, and function in health and disease. *J Cell Physiol* 233(9):6425–6440.
https://doi.org/10.1002/jcp.26429
38. Ferrante CJ, Leibovich SJ (2012) Regulation of macrophage polarization and wound healing. *Adv Wound Care* 1(1):10–16.
https://doi.org/10.1089/wound.2011.0307
39. Qu XH, Wang MQ, Wang MC et al (2022) Multi-mode antibacterial strategies enabled by gene-transfection and immunomodulatory nanoparticles in 3D-printed scaffolds for synergistic exogenous and endogenous treatment of infections. *Adv Mater* 34(18): e2200096.
https://doi.org/10.1002/adma.202200096
40. Wang CL, Yang YJ, Wang N et al (2025) Design and application of antimicrobial nanomaterials in the treatment of periodontitis. *Nanomedicine* 20(7):707–723.
https://doi.org/10.1080/17435889.2025.2469492
41. Sha WJ, Zhao B, Wei HZ et al (2023) Astragalus polysaccharide ameliorates vascular endothelial dysfunction by stimulating macrophage M2 polarization via potentiating Nrf2/HO-1 signaling pathway. *Phytomedicine* 112:154667.
https://doi.org/10.1016/j.phymed.2023.154667
42. Das A, Sinha M, Datta S et al (2015) Monocyte and macrophage plasticity in tissue repair and regeneration. *Am J Pathol* 185(10):2596–2606.
https://doi.org/10.1016/j.ajpath.2015.06.001
43. Johnson BZ, Stevenson AW, Prêle CM et al (2020) The role of IL-6 in skin fibrosis and cutaneous wound healing. *Biomedicines* 8(5):101.
https://doi.org/10.3390/biomedicines8050101
44. Short WD, Steen E, Kaul A et al (2022) IL-10 promotes endothelial progenitor cell infiltration and wound healing via STAT3. *FASEB J* 36(7):e22298.
https://doi.org/10.1096/fj.201901024RR
45. Lin ZQ, Kondo T, Ishida Y et al (2003) Essential involvement of IL-6 in the skin wound-healing process as evidenced by delayed wound healing in IL-6-deficient mice. *J Leukoc Biol* 73(6): 713–721.
https://doi.org/10.1189/jlb.0802397